Turbulent Flows With Drops and Bubbles: What Numerical Simulations Can Tell Us— Freeman Scholar Lecture

Giovanni Soligo
Institute of Fluid Mechanics and Heat Transfer,
TU Wien,
Vienna 1060, Austria;
Complex Fluids and Flows Unit,
Okinawa Institute of Science and Technology,
Graduate University,
Okinawa 904-0495, Japan

Alessio Roccon
Institute of Fluid Mechanics and Heat Transfer,
TU Wien,
Vienna 1060, Austria;
D.P.I.A.,
University of Udine,
Udine 33100, Italy

Alfredo Soldati[1]
Institute of Fluid Mechanics and Heat Transfer,
TU Wien,
Vienna 1060, Austria;
D.P.I.A.,
University of Udine,
Udine 33100, Italy
e-mail: alfredo.soldati@tuwien.ac.at

Turbulent flows laden with large, deformable drops or bubbles are ubiquitous in nature and a number of industrial processes. These flows are characterized by physics acting at many different scales: from the macroscopic length scale of the problem down to the microscopic molecular scale of the interface. Naturally, the numerical resolution of all the scales of the problem, which span about eight to nine orders of magnitude, is not possible, with the consequence that numerical simulations of turbulent multiphase flows impose challenges and require methods able to capture the multiscale nature of the flow. In this review, we start by describing the numerical methods commonly employed and by discussing their advantages and limitations, and then we focus on the issues arising from the limited range of scales that can be possibly solved. Ultimately, the droplet size distribution, a key result of interest for turbulent multiphase flows, is used as a benchmark to compare the capabilities of the different methods and to discuss the main insights that can be drawn from these simulations. Based on this, we define a series of guidelines and best practices that we believe to be important in the analysis of the simulations and the development of new numerical methods. [DOI: 10.1115/1.4050532]

1 Introduction

Turbulent multiphase flows are ubiquitous in nature and our everyday life. These flows play a key-role in various applications, from geophysical phenomena [1,2], to food [3,4], and industrial processes [5,6]. In addition, never as in this year, was so clear how important are multiphase flow processes also in host-to-host airborne disease transmission [7–13]. Compared to single-phase turbulence, the study and mathematical modeling of multiphase turbulence are much more complex, since they require the description of an ever-moving and deforming interface, of its topological modifications, and the underlying turbulent flow. In addition, and possibly in the vast majority of processes, the phases are not pure but carry small quantities of surface-active agents (surfactants) that modify globally and locally interface properties. These agents, composed of a hydrophilic head and a hydrophobic tail, collect at the interface between the phases and act primarily by reducing the local surface tension value, thus decreasing the normal interfacial stresses. However, when surfactants are not uniformly distributed, they give rise to surface tension gradients and thus to stresses tangential to the interface (Marangoni stresses [14]), further increasing the complexity of the interactions [15–17].

Multiphase turbulence is a nontrivial problem and is governed by a physics acting on a wide range of scales: from the largest problem scale, down to the Kolmogorov scale of turbulence and further down to the molecular scale of the interface. Such a diversity of scales can be appreciated from Fig. 1, which shows a rendering of a turbulent flow laden with surfactant-covered drops/bubbles (drops hereinafter without any loss of generality). The main panel shows the macroscopic scales of the system: in general, these are the largest turbulence scales (i.e., the size of a duct or the diameter of a jet). The mesoscopic scales can be

appreciated in the first close-up view (top-left lens): the typical size of the drops and the smaller turbulent structures. The second close-up view (top-right lens) shows the nanoscopic scales, including the molecular scale of interfacial phenomena and of surfactants (here represented as amphiphilic molecules with a blue hydrophilic head and yellow hydrophobic tails), which are dominated by a physics acting at the molecular level [18]. Figure 1 shows, in a nutshell, the complexity of the problem: although the length scales cover about eight to nine orders of magnitude and are thus largely separated, phenomena acting at each different scale are tightly intertwined and have a strong effect on the other scales.

Obtaining accurate predictions on the behavior of the system is extremely important for the optimization and improvement of many processes and applications. However, assessing information on physical quantities of interest in multiphase turbulence is complex: experimental measurements on multiphase flows are a challenging task [19–21] and accurate simulations of multiphase flows require methods able to capture the topology of the dispersed phase and its modifications [22–24]. In addition, the presence of surfactants or contaminants makes this task even more challenging and requires the creation of more sophisticated experimental [25,26] and numerical [27–30] techniques. Simulations are an essential tool to investigate the physics of multiphase turbulence and are becoming increasingly popular in recent years: numerical simulations allow to access detailed space- and time-resolved information on the flow field, on the dispersed phase morphology, and the surfactant distribution. Starting from the pioneering work of Harlow and Welch [31], different methods have been developed to numerically investigate multiphase flows [22–24,32]. However, despite all the recent advancements, a common issue dictated by the multiscale nature of multiphase turbulence affects the reliability of simulations: the limited spatial and temporal resolution one can reasonably afford [33]. In particular, as done for single-phase turbulence [34,35], it would be highly desirable to perform simulations in which all scales are directly resolved, without any model. Unfortunately, this approach cannot be applied to multiphase flows since the scale separation between the
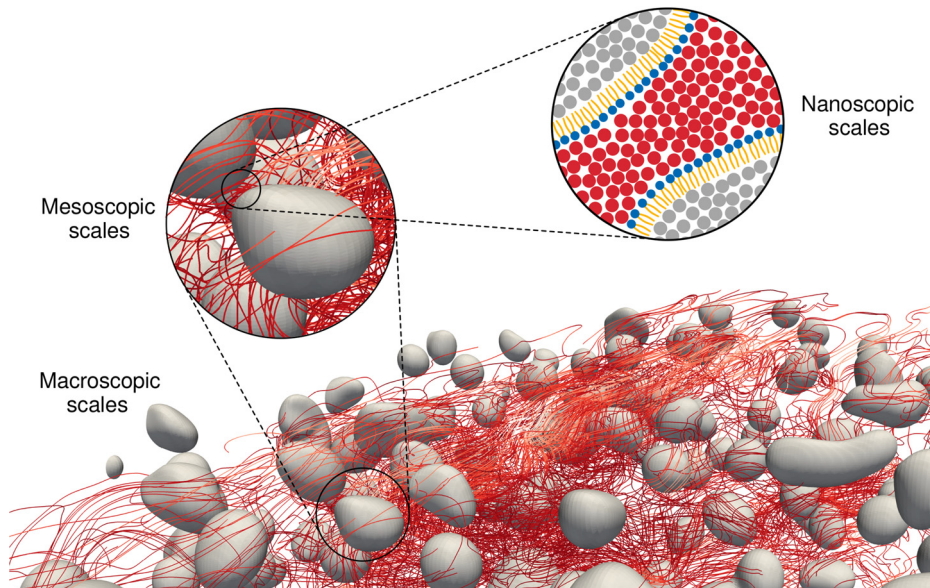
Fig. 1 Qualitative rendering showing the wide range of scales involved in the physics of turbulent multiphase flows. The main panel highlights the macroscopic scales, such as the large flow structures and the clusters of drops. In the first close-up view, the top-left lens, the mesoscopic scales, the typical size of drops, and the smaller turbulent eddies, are reported, while in the second close-up view, the top-right lens, the interfacial molecular scales are shown. At the molecular scale, the different fluids are represented, respectively, as gray and red molecules, while surfactant is depicted as amphiphilic molecules, with a hydrophilic head (blue) and hydrophobic tails (yellow). (See color figure online).

largest flow scale and the smallest interfacial scale is about eight to nine orders of magnitude, while the most recent high-performance computing infrastructures can handle a maximal scale separation of about three to four orders of magnitude. Besides, although most of the numerical approaches for the simulation of multiphase flows rely on the continuum hypothesis, as length scales become smaller and smaller, the continuum hypothesis breaks down and molecular-scale dynamics have to be considered [22,36].

The impossibility to resolve all the length scales using a unique set of governing equations has driven researchers to the development of different families of computational methods, which can be classified based on the range of resolved scales and the characteristic size of the simulated drop. In Fig. 2, the characteristic size of the drop is reported on the horizontal axis, while the range of resolved scales is reported on the vertical axis. The vertical and horizontal gray bands show the range of values of the Kolmogorov length scale for typical direct numerical simulations of turbulence. Starting from the bottom left, we have molecular dynamics simulations (red box), where all the nanoscopic scales are resolved and thus all the interactions among drops and surfactant molecules are directly resolved as well. Clearly, the characteristic size of the drop that can be simulated is very small [37,42,43] (less than 1 micrometer) and turbulence is not considered. Increasing the characteristic drop/bubble size and the range of scales resolved, we find Lagrangian particle tracking (LPT) methods (black box). In these methods, all turbulence scales are resolved and drops are assumed as pointwise and must be smaller than or of the order of the Kolmogorov scale [38,44,45]. The motion of the drops is modeled using a set of force- and torque-balance equations, while drops feedback on the fluid, drop-drop interactions, and possibly drop deformation are accounted for with specific phenomenological models. Keeping the same range of resolved scales but increasing the characteristic drop size, we have interface-resolved simulation methods [22–24] (blue box), which are the focus of this review. Within this class of methods, we can make a distinction based on the approach used to describe the interface: interface tracking methods, which explicitly follow

the interface (using, for example, sets of marker points or interface-fitted grids) and interface capturing methods, which implicitly define the interface using a constant value of a color function (i.e., an equivalent phase-concentration field). Also for this class of methods, the entire range of turbulence scales is resolved. To extend the range of drop sizes that can be described, the latter two classes of methods (interface-resolved simulations and LPT) can be coupled obtaining hybrid approaches [40,46,47] (yellow box). This family of methods uses interface-resolved methods to describe the dynamics of the larger–scale interfaces (e.g., larger drops), while the motion of the smaller drops is simulated using an LPT approach. Specific algorithms are used to switch between the interface-resolved description and the Lagrangian pointwise-particle tracking depending on the size of the drops, which can change upon breakage or coalescence events. Finally, shifting upward the range of resolved scales, we have the large eddy simulations (LES) with subgrid surface dynamics (SGSD) [41,48,49] (gray box). This class of methods uses subgrid models to describe the dynamics of the smaller turbulence scales, of the smaller drops, and of the subgrid interfacial features. In particular, a subset of these methods adopts closure models for the velocity field [41,49], while interfacial phenomena are resolved on the same grid or a more refined grid; conversely, another subset of methods use closure models for both subgrid turbulence scales and subgrid interfacial features [48].

In this review, we focus on direct numerical simulations of multiphase turbulence performed using interface-resolved methods (blue box). The term direct numerical simulation is here used to identify *fully verified simulations of validated equations, where all continuum time and length scales are fully resolved for an unsteady flow involving a large range of flow scales* [50]. We restrict our discussion to isothermal, noncondensing, nonevaporating multifluid systems. We start by describing the numerical methods commonly employed for interface-resolved simulations in Sec. 2; this part is divided into three sections, dedicated, respectively, to the flow, interface, and surfactant simulation methods. Then, we focus on the main challenges and critical aspects of the different simulation methods. Specifically, we discuss the impact
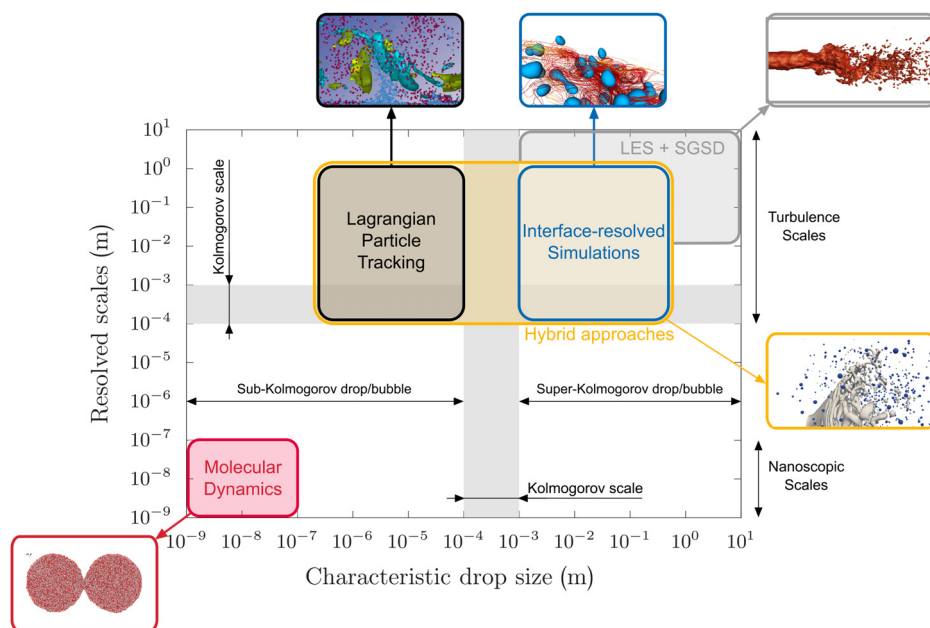
Fig. 2 Classification of the families of methods commonly used for the description of turbulent dispersed multiphase flows. The families of methods are classified depending on the range of drop size described and the range of scales resolved (indicated in meters). The typical Kolmogorov length-scale range (for the Reynolds numbers commonly simulated) is reported with a gray band. Adapted from Perumanath et al. [37] (molecular dynamic); Soldati et al. [38] (Lagrangian particle tracking); Roccon et al. [39] (interface-resolved simulations); Evrard et al. [40] (hybrid approaches); and Xiao et al. 2014 [41] (LES + subgrid surface dynamics).

of the multiscale nature of these flows on the reliability of the numerical representation of coalescence and breakage events and the smaller droplets and ligaments, Sec. 3. We then consider the drop size distribution as a benchmark to compare the capabilities of the different methods, Sec. 4. This result is of key interest in many applications and can be seen as the ultimate competition between coalescence and breakage events (and their numerical representation). This comparison allows us to discuss the main weaknesses of the different simulation methods and which improvements can be adopted to mitigate these issues. Finally, we define a series of guidelines and best practices that we believe should be always kept in mind in the analysis of simulation results and the development and validation of new numerical methods, Sec. 5.

2 Numerical Description of Multiphase Flows

The simulation of turbulent multiphase flows requires numerical tools able to describe the different aspects of the system. In the following, each of these aspects will be addressed separately, starting from the description of the flow field in each phase and of the coupling of the phases at the interface, Sec. 2.1. Then, the numerical methods used to track the movement and shape of the interface in space and time will be introduced, with a particular focus on whether and how each numerical method is able to simulate merging and coalescence of the interface, Sec. 2.2. Finally, we address the numerical method used to track the concentration of a surfactant phase at the interface for different types of surfactant (i.e., soluble and insoluble surfactants), Sec. 2.3.

2.1 Flow Field Description. The description of the flow field requires numerical methods that can handle abrupt changes of density and viscosity at the interface and that can account for the presence of surface tension forces [23]. The oldest and more widely adopted approach is the one-fluid approach, which relies on the solution of a single set of Navier–Stokes equations in the

entire domain (usually performed on a structured grid). Possible alternatives to this approach are the body-fitted grid methods [51–54], which rely on the solution of multiple sets of Navier–Stokes equations, one for each phase, coupled at the interface. A third possible solution, which attempts at combining the advantages of the one-fluid approach with the accuracy of the body-fitted grid methods is the class of the sharp-interface methods [55–59]. These methods rely on the solution of the Navier–Stokes equations in separated domains using structured grids, which are easier to handle; halo regions are used to couple the separate domains. A schematic classification of the different methods is shown in Fig. 3.

2.1.1 One-Fluid Approach. In the framework of the one-fluid approach, a single set of Navier–Stokes equations is used to obtain the flow field solution on the entire domain
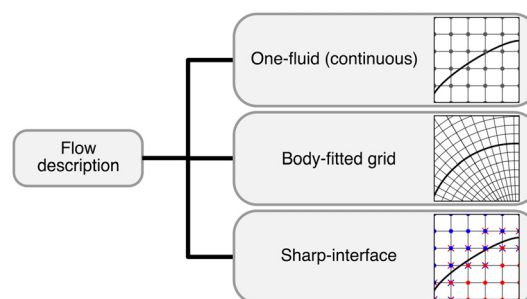

Fig. 3 Numerical methods commonly used for the description of the flow field. From top to bottom: (i) one-fluid (or continuous) approach, one set of Navier–Stokes equations are solved in the entire domain; (ii) body-fitted grid methods, multiple sets of Navier–Stokes equations are solved on structured grids conformed to the phase boundaries and coupled at the interface; and (iii) sharp-interface approach, multiple sets of Navier–Stokes equations are solved and coupled on single a structured grid.

$$\frac{\partial(\rho\mathbf{u})}{\partial t} + \nabla \cdot (\rho\mathbf{u}\mathbf{u}) = -\nabla p + \nabla \cdot (\eta\nabla\mathbf{u}) + \mathbf{F}_\sigma + \mathbf{F}_b \quad \text{in } \Omega \quad (1)$$

where $\mathbf{u}$ is the velocity, p is the pressure, ρ and η are, respectively, the local density and viscosity, $\mathbf{F}_\sigma$ are the surface tension forces, $\mathbf{F}_b$ the body forces and Ω is the computational domain. The Navier–Stokes equations are modified so to account for density and/or viscosity jumps between the two phases. Surface tension forces are introduced to satisfy kinematic and dynamics boundary conditions at the interface [60]. In particular, density and viscosity fields are usually expressed in term of Heaviside functions $\mathcal{H}$ and the density (viscosity) ρ_1 and ρ_2 (η_1 and η_2) of the two phases

$$\begin{aligned}\rho &= \rho_1 + \mathcal{H}(\rho_2 - \rho_1) \\ \eta &= \eta_1 + \mathcal{H}(\eta_2 - \eta_1)\end{aligned} \quad (2)$$

while surface tension forces are introduced using delta functions [23,61]. The numerical resolution of discontinuities of these fields at the interface requires the development of specific smoothing kernels that can smear out density and viscosity jumps across the interface and surface tension forces to a point that can be numerically handled (two or more grid points [62]). Handling these discontinuous functions poses several challenges: for larger density/viscosity contrasts, solvers capable of dealing with large variations of the physical properties are required [63–68], while for surface tension forces, robust models suitable to accurately describe these forces in a wide range of multiphase flow problems are sought [61,69–71]. Overall, this approach is the most adopted since it allows for the use of highly parallel and efficient solvers, similar to those commonly used for the resolution of single-phase flows on structured grids [23,64]. The main limitations of this class of methods are represented by the smoothing of the discontinuities across the interface, which can limit the accuracy of the method, and the need for schemes able to accurately handle large density and viscosity variations.

2.2 Body-Fitted Grid Methods. This class of methods exploits grids that conform to the interface separating the fluids: this method largely simplifies the imposition of the boundary conditions at the interface [51–54,72]. As shown in Eq. (3), the flow field solution is usually obtained via the solution of two (or more) sets of Navier–Stokes equations, one for each fluid domain (subscripts 1 and 2 in Eq. (3)), and coupled at the interface (see also the scheme in Fig. 3)

$$\begin{aligned}\frac{\partial(\rho_1\mathbf{u}_1)}{\partial t} + \nabla \cdot (\rho_1\mathbf{u}_1\mathbf{u}_1) &= -\nabla p_1 + \nabla \cdot (\eta_1\nabla\mathbf{u}_1) + \mathbf{F}_{b,1} \quad \text{in } \Omega_1 \\ \frac{\partial(\rho_2\mathbf{u}_2)}{\partial t} + \nabla \cdot (\rho_2\mathbf{u}_2\mathbf{u}_2) &= -\nabla p_2 + \nabla \cdot (\eta_2\nabla\mathbf{u}_2) + \mathbf{F}_{b,2} \quad \text{in } \Omega_2\end{aligned}$$
$$(3)$$

Here $\Omega = \Omega_1 \cup \Omega_2$ is the entire computational domain, while Ω_1 and Ω_2 are the subdomains occupied by each phase. Suitable boundary conditions for each phase couple the two separate subdomains at the interface; jump conditions for the velocity field or any other fluid property can be directly applied. Despite the improved accuracy offered by this class of methods, the use of structured grids limits its applicability to drops undergoing small deformations without breaking. In addition, if the problem involves a large number of drops, the grid generation becomes computationally expensive [23,73], and therefore this approach is usually limited to simpler problems.

2.2.1 Sharp-Interface Methods. Sharp interface methods [23,55–59,74] are an alternative class of approaches that try to combine the advantages of the fixed structured grid, typical of the one-fluid formulation, with the accuracy given by the interfacial jump conditions, typical of the body-fitted grid approach. Among the possible implementations [55–59,74,75], the ghost-fluid

method [58,74,76,77] has emerged as the most popular. In the framework of the ghost-fluid method, two sets of Navier–Stokes equations (one for each phase, subscripts 1 and 2)

$$\begin{aligned}&\frac{\partial(\rho_1\mathbf{u}_1)}{\partial t} + \nabla \cdot (\rho_1\mathbf{u}_1\mathbf{u}_1) \\ &= -\nabla p_1 + \nabla \cdot (\eta_1\nabla\mathbf{u}_1) + \mathbf{F}_{b,1} \quad \text{in } \Omega_1 \cup \Omega_{1,\text{ghost}} \\ &\frac{\partial(\rho_2\mathbf{u}_2)}{\partial t} + \nabla \cdot (\rho_2\mathbf{u}_2\mathbf{u}_2) \\ &= -\nabla p_2 + \nabla \cdot (\eta_2\nabla\mathbf{u}_2) + \mathbf{F}_{b,2} \quad \text{in } \Omega_2 \cup \Omega_{2,\text{ghost}}\end{aligned}$$
$$(4)$$

are solved in the respective domains and ghost nodes ($\Omega_{1,\text{ghost}}$ and $\Omega_{2,\text{ghost}}$, marked with crosses in the respective scheme of Fig. 3) are used to improve the treatment of the discontinuities at the interface [58,74]. The two Navier–Stokes equations are solved separately in each subdomain ($\Omega_1 \cup \Omega_{1,\text{ghost}}$ and $\Omega_2 \cup \Omega_{2,\text{ghost}}$, respectively), using the ghost nodes across the interface to impose the jump conditions on the velocity field and the phase properties. In this way, standard single-phase solvers can be used, and jump conditions at the interface between the two fluids can be imposed explicitly. The capability of handling discontinuities at the interface allows for a straightforward simulation of complex interfacial conditions, such as phase-change [78–80]. Sharp-interface methods appear to be promising and suitable for a wide range of multiphase flow instances [81–86]. There are however some issues that limits their application, among which the discretization of the viscous terms [77,87] and the much higher computational cost with respect to the more commonly adopted one-fluid approach.

2.3 Interface Description: Interface Tracking and Interface Capturing. The simulation of a moving, ever-deforming interface, which can also undergo topological changes, is a challenging task that requires accurate and robust algorithms. The available methods can be classified into two families, interface tracking and interface capturing methods; a synthetic classification listing the most popular methods is reported in Fig. 4. The fundamental difference resides in the definition of the interface: interface tracking approaches explicitly follow the position of the
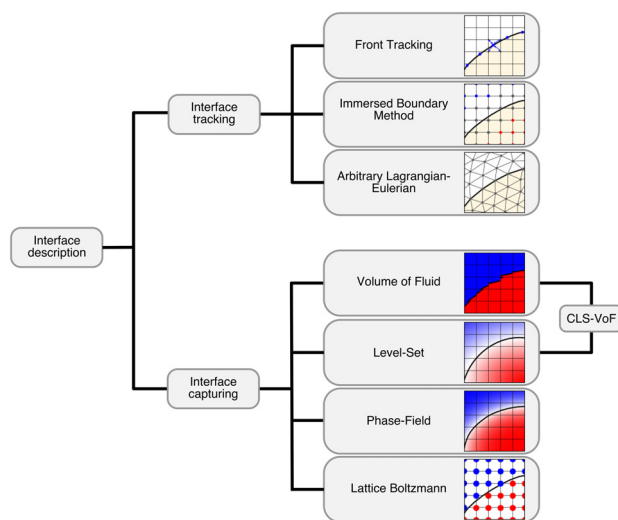

Fig. 4 Numerical methods employed for the description of the dispersed phase topology. The methods can be classified into interface tracking methods, which rely on Lagrangian markers or interface-fitted meshes and interface capturing methods, which rely on color functions or phase concentration fields. Among the interface tracking methods, we have: (i) FT method; (ii) IBM; (iii) ALE method. In the category of the interface capturing methods we have: (i) VoF; (ii) LS method; (iii) phase-field (PF) method; and (iv) LB method.
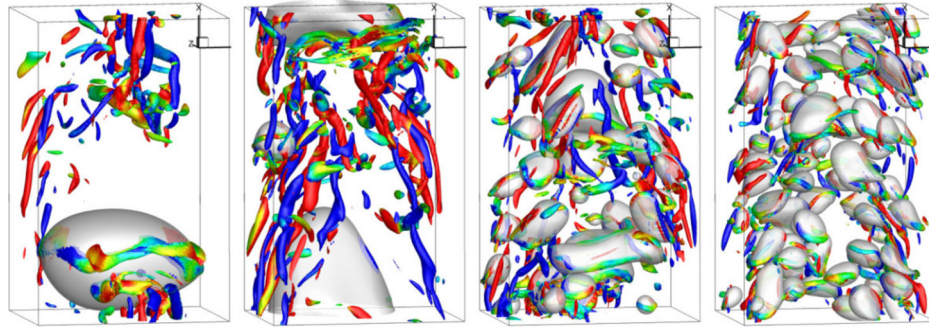
Fig. 5 Front Tracking simulation of a vertical channel flow laden with buoyant bubbles; the vortical structures, identified using the λ_2 method and colored according to their orientation, are also reported. Here the effect of topological modifications of the interface (namely, breakage and coalescence) is investigated; fronts are reconnected when they are closer than a set distance. Adapted from Lu and Tryggvason [91]. (See color figure online).

interface with Lagrangian markers or interface-fitted meshes, while interface capturing methods define the interface position as a prescribed value of a color function or phase-concentration field. The definition of the interface has direct consequences on the simulation of topological changes of the interface (as, for instance, breaking and merging): interface tracking methods require explicit models to manage the connectivity of Lagrangian markers or meshes, while topological modifications of the interface are implicitly handled in interface capturing methods. As will become clear later on, there is yet no common agreement on which is the best way to describe topological changes, and each family of methods has its advantages and disadvantages.

2.3.1 Interface Tracking Methods

2.3.1.1 Front tracking. This method was developed and largely exploited by Unverdi and Tryggvason [88] for the description of incompressible multiphase viscous flows; the capabilities of the method were demonstrated with two- and three-dimensional simulations of bubble motion and interaction. This approach relies on the advection of a set of Lagrangian markers that define the instantaneous position of the interface (blue dots in Fig. 4). The Lagrangian markers, denoted by $\mathbf{x}_f$, are advected according to the local flow velocity, $\mathbf{u}$, as follows:

$$\frac{\partial \mathbf{x}_f}{\partial t} = \mathbf{u} \tag{5}$$

Each connected set of marker points defines a separate interface; as the interface shrinks and expands, the linked list of points is then updated at simulation run-time by adding or removing marker points when needed. For instance, a marker point might be added when the distance between adjacent points exceeds a certain threshold or might be removed when the distance decreases below a minimum distance. The restructuring of the front by adding or deleting marker points allows to keep an adequate resolution of the interface (by adding marker points when the interface stretches) and to avoid wiggles of the interface much smaller than the grid size (by deleting marker points when the interface shrinks) [89]. This restructuring of the interface acts only on each separate set of connected markers, i.e., on every single interface. This means that interactions among separate interfaces (i.e., separate sets of linked points), which may lead to coalescence (merging of two or more sets of linked points) or breakage (creation of new sets of linked points) phenomena, must be handled with additional ad hoc models. To address this issue, different strategies to deal with topological modifications of the interface have been proposed: separate interfaces can be merged when they are closer than a certain minimum distance (e.g., the grid size [89–92]), when they stay close enough for a time longer than a prescribed

interaction time [93] or using more sophisticated algorithms [94–96] (Fig. 5).

2.3.1.2 Immersed boundary method. This method was first proposed in the 1970s by Peskin in his Ph.D. thesis [97] for the numerical simulation of flow patterns around heart valves. The immersed boundary method (IBM) finds huge and important application in the simulation of flows past solid objects, bounded by complex and possibly moving boundaries [98,99] or laden with dense suspensions of finite-size particles [100–102]. Relatively fewer works can be found for flows involving fluid–fluid interfaces [103–108]. In this method, the interface is represented by a moving Lagrangian mesh (gray nodes in Fig. 4); an additional forcing term, which accounts for the interface contribution, is applied to the Navier–Stokes equations only in the grid cells crossed by the interface. A smoothing kernel defines the way in which the forcing is applied on the neighboring grid nodes. Immersed boundary methods, similarly to front tracking (FT) methods, become computationally complex when a large number of separate interfaces is simulated: a separate set of Lagrangian markers, with their relative connectivity information, has to be tracked in space and time and collisions among different interfaces, and the eventual topological modifications of the interface, have to be accounted for. Some of these issues were tackled by Spandan et al. [106], including a collision detection algorithm; however, according to the available literature, topological modifications of the interface have not yet been tackled and are indeed among the possible future developments.

2.3.1.3 Arbitrary Lagrangian–Eulerian. This method was initially developed also in the 1970s by Hirt and coworkers [109] for the simulation of fluid–solid interactions and shocks. In the frame of this approach the mesh can move with the fluid (Lagrangian), or also can be maintained fixed (Eulerian) or even move with any other prescribed speed (mixed Lagrangian-Eulerian) [109]. In the simulation of multiphase flows, a body-conforming mesh is often adopted [110–114]: the grid lines are aligned with the interface in between the phases. In this way jump conditions at the interface can be directly applied in a simple way, without introducing forcing terms or smoothing operators. This approach, however, requires frequent mesh movement and remeshing operations; Cheng et al. [114] presented an accurate, efficient, and robust mesh generator suitable for arbitrary Lagrangian–Eulerian (ALE) approaches. They tested the performances of the proposed method against several benchmark cases, among which the magnitude of spurious current at the interface of a steady drop and the drop formation and detachment from a dripping faucet. ALE methods were developed to combine the advantages of Lagrangian and Eulerian formulations [113]. This feature comes however at the additional cost of frequent remeshing, which can introduce changes in the mass of each phase. In particular, Anjos et al. [113]

observed that the error in the conservation of mass grows with the magnitude of interface deformation, despite the use of mass correction schemes. Hybrid approaches have also been proposed, as, for example, a hybrid coupled level-set (LS) and volume of fluid (CLS-VoF) and ALE approach [115]. In this approach the interface is captured with the CLS-VoF method, then its evolution (level-set and volume of fluid functions) is computed with the ALE approach.

2.3.2 Interface Capturing Methods

2.3.2.1 Volume of fluid. This method was first developed by Hirt and Nichols [116] as a more efficient and flexible approach for the simulation of problems involving free boundaries. The capability and robustness of the method were shown on several benchmark problems, among which the rotation of a slotted disk, the dam-breaking problem, and the Rayleigh–Taylor instability [22,116,117]. This approach is based on the advection of a phase indicator function ϕ

$$\frac{\partial \phi}{\partial t} + \nabla \cdot (\mathbf{u}H) = \phi \nabla \cdot \mathbf{u} \qquad (6)$$

which represents the local concentration of each phase (cell-average of the indicator function H). The indicator function H is equal to zero in one phase and to one in the other phase. VoF methods can be further categorized in algebraic and geometric approaches. Algebraic VoF methods [116] do not involve any interface reconstruction step and directly compute the fluxes; the profile of the phase indicator across the interface is imposed (for instance, a hyperbolic tangent function in tangent of hyperbola for interface capturing (THINC) schemes [118]). Algebraic approaches have a lower computational cost with respect to geometric approaches; their accuracy is, however, slightly lower. Geometric approaches, on the other hand, require an interface-reconstruction step. The newer second-order-accurate piecewise linear interface calculation scheme [119] is the most used and is usually preferred to the older and first-order-accurate simple line interface calculation [120] and solution algorithm (SOLA-VoF) [116]. The geometric reconstruction of the interface improves the accuracy in the calculation of the fluxes and the advection of the interface. In the VoF framework, topology modifications of the interface (e.g., merging and breakage of the interface) are implicitly described, as in all interface capturing approaches (Fig. 6).

$t' = 2$ $t' = 2.5$

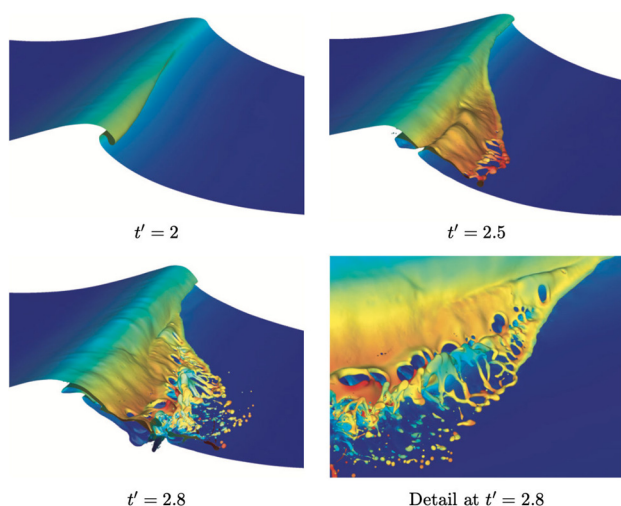$t' = 2.8$ Detail at $t' = 2.8$

Fig. 6 Numerical simulation of the time-evolution of a Stokes wave in an air–water system. The interface is described using a geometric VoF coupled to an adaptive mesh refinement algorithm to better capture the dynamics of small droplets and thin ligaments during the breaking of the wavefront. Adapted from Fuster et al. [121].

2.3.2.2 Level-set. This method was initially developed as an alternative to SLIC-based (simple line interface calculation) VoF approaches, as they allow for a more accurate calculation of the curvature of the front (interface) [122]. Osher and Sethian [122] devised a numerical approach for the simulation of fronts propagating with curvature-dependent speed; this method was then further developed in the current level-set formulations [122–124]. The recent review by Gibou et al. [125] covers the most recent advances on level-set approaches, their numerical approximation, and their applications. Level-set approaches rely on a smooth color function to define the dynamics of each phase; the smoothness of this function allows for a highly accurate computation of interface normals and curvature, which are crucial for the computation of surface tension forces [61]. In addition, being an interface capturing approach, topological modifications of the interface are automatically captured. In the classic level-set approach the color function ϕ is a signed-distance function and its zero-level identifies the position of the interface; its evolution is obtained by solving the equation

$$\frac{\partial \phi}{\partial t} + \mathbf{u} \cdot \nabla \phi = 0 \qquad (7)$$

The main issue associated with this approach is the problem of maintaining the signed-distance property of the color function: specific advection schemes [23,126,127] and reinitialization of the color function are required [62,70,128–130]. During the reinitialization process, the mass of each phase is not conserved and mass losses may occur; while a finer grid may mitigate this issue [125,131], discrete mass conservation for each phase is still not granted [32]. Olsson and Kreiss [132] developed the conservative level-set (CLS) approach; here the signed-distance color function is replaced by a hyperbolic tangent profile, similar to the color function adopted in phase-field (PF) methods. The CLS approach consists of two steps: an advection stage and a reinitialization stage. In the first stage, the level-set function is advected as in the classic formulation; during this stage, the color function may loose its hyperbolic tangent profile and has to be reinitialized. The reinitialization stage is the substantial difference from the classic LS approaches: during this step in CLS approaches, not only the color function is restored (as in classic LS approaches), but the mass of each phase is restored as well, thus eliminating the mentioned mass-conservation problems.

2.3.2.3 Coupled level-set and volume of fluid (CLS-VoF). To improve mass conservation, LS approaches have also been coupled to VoF methods [133,134]: the high accuracy in the computation of geometrical properties of the interface (normals and curvature) typical of LS methods is combined with the mass conservation of VoF approaches. The coupled level-set and volume of fluid (CLS-VoF) methods have higher accuracy with respect to level-set or volume of fluid approaches; this higher accuracy, however, comes at a higher computational cost. Within this approach, accurate algorithms can be adopted to advect the local volume fraction (integral of the level-set color function over the computational cell), so that mass conservation is achieved, while normals and curvature of the interface are computed from the level-set function, so that higher accuracy is obtained. The level-set function is updated starting from the volume of fluid marker function and the level-set function at the previous time-step. This approach, thus, allows for accurate computation of surface tension forces (as in all LS methods) and, at the same time, it is mass conserving (as in all VoF methods).

2.3.2.4 Phase-field. This method was first developed in the late 1950s by Cahn and Hilliard [135–137] for critical and near-critical mixtures and was later extended to consider multifluid systems far from critical conditions [138–141]. Earlier formulations were limited to phases with matched density and viscosity, and have been then extended to the simulation of flows with density

[142,143] or viscosity [39,143] contrasts. The PF approach is based on a thermodynamically derived Ginzburg–Landau free energy functional $\mathcal{F}$, which is composed of the sum of two different contributions (two-phase systems). The first contribution, f_0, accounts for the tendency of the system to separate into the two pure phases, while the second contribution, f_{mix} (mixing energy), is a nonlocal term accounting for the energy stored at the interface

$$\mathcal{F} = \int_\Omega (f_0 + f_{\text{mix}})\mathrm{d}\Omega \qquad (8)$$

where Ω is the domain considered. From this free-energy functional two different gradient-flow formulations, the Allen–Cahn and the Cahn–Hilliard, can be obtained. The first formulation mainly finds application in the simulation of solidification and melting processes [144], while the latter is commonly used in the simulation of multiphase flows. In the most general form, the Cahn–Hilliard formulation reads as

$$\frac{\partial \phi}{\partial t} + \mathbf{u} \cdot \nabla \phi = \nabla \cdot \left(\mathcal{M}_\phi \nabla \mu_\phi \right) \qquad (9)$$

where ϕ is the phase-field (i.e., the phase indicator), $\mathcal{M}_\phi$ the phase-field mobility and $\mu_\phi = \delta\mathcal{F}/\delta\phi$ the chemical potential, obtained as the variational derivative of the free energy functional. This approach is exact for critical and near-critical mixtures, which are characterized by a finite thickness of the interface, while it is approximated for far-from-critical mixtures [138,139]. Indeed, at the molecular level, an actual interface is a finite-thickness transition layer in between the bulk of the pure phases; in the framework of the PF method, the interface is considered as a finite-thickness smooth transition layer as well, although it is much thicker than a real interface. Indeed, the grid resolution controls the thickness of the interface [145]. The color function defining the distribution of each phase, the phase-field variable, is proportional to the local concentration of each phase (C_1 and C_2, respectively): it is constant in the bulk of each phase and undergoes a smooth transition across the interface following a hyperbolic tangent profile:

$$\phi = \frac{C_1 - C_2}{C_1 + C_2} = \begin{cases} +1 & \text{in phase 1} \\ 0 & \text{at interface} \\ -1 & \text{in phase 2} \end{cases} \qquad (10)$$

This interfacial profile corresponds to the equilibrium solution obtained from the free energy functional. Due to the energy minimization principle on which the PF method is based, some issues arise in the simulation of multiphase flows, namely, shrinkage and coarsening phenomena. Shrinkage phenomena can occur whenever the interfacial profile is perturbed from its equilibrium solution: restoration of the equilibrium profile can introduce mass leakages among the phases [146]. While the total mass is conserved, the mass of each phase is not necessarily conserved by the method. An out-of-equilibrium profile, e.g., perturbed by the local flow, can also lead to inaccuracies in the computation of surface tension forces. Coarsening phenomena do not depend on possible perturbations of the interfacial profile and are instead rooted in the energy minimization principle: larger domains of one phase can grow at the expense of smaller domains of the same phase. This way, the total interfacial energy is reduced. To circumvent these drawbacks, corrected formulations have been proposed [147–149]; it must be noted, however, that these formulations are no longer gradient flows of the Ginzburg–Landau free energy functional, and thus they have to be considered as a mean-field approximation [150]. In their papers, Mirjalili et al. [32,151] compared the accuracy, computational cost, and order of convergence of two state-of-the-art VoF and PF solver. They observed that the VoF solver has a higher accuracy than the PF approach at the same resolution,
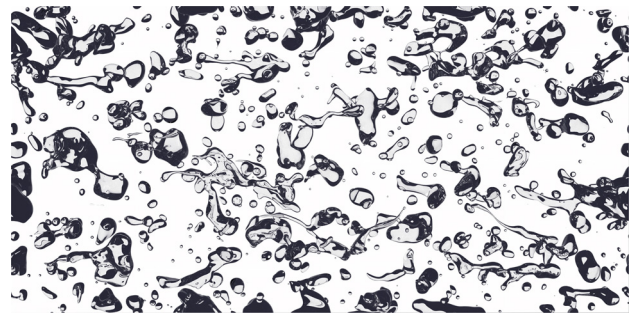

Fig. 7 Rendering of a swarm of drops released in a turbulent channel flow. The simulation has been performed using a phase-field method (Cahn-Hilliard formulation) to describe the interface dynamics. Details on the simulation setup can be found in Soligo et al. [152].

however, the PF approach has a consistently lower computational cost. Both methods showed a similar order of convergence (Figs. 7 and 8).

2.3.2.5 Lattice Boltzmann. The origin of this class of methods is based on the kinetic theory of gases [154–160]. Mass, momentum, and energy conservation equations are derived from the discrete Boltzmann equation, which describes the advection and collision dynamics of a particle probability distribution function. Particles are located on a regular lattice and can jump on different sites according to a finite set of possible discrete particle velocities. The lattice Boltzmann (LB) approach is a particle method and therefore it has the potential advantage of describing interfacial phenomena in a more straightforward way compared to continuum-based approaches. However, in most of the currently used formulations, molecular interactions are not directly described by LB methods and interfacial dynamics are described via phenomenological thermodynamical models, and capillary effects are introduced through density gradients approaches, as in continuum-based methods [161]. Four different approaches can be identified within the LB framework for the simulation of multiphase flows [162–165]: the color-fluid model [166–168], the interparticle-potential model [169–171], the free-energy model [172,173], and the mean-field theory model [174–176]. The color-fluid model uses two different particle distribution functions (i.e., red and blue particles) to distinguish the two phases; surface tension is introduced as an additional collision operator, while phase separation is obtained through a segregation step that forces particles into regions of the same color. The interparticle-potential model is based on a nearest-neighbor interaction concept: the collision operator is modified to account for short range particle–particle interactions. With this modification, surface tension is implicitly accounted for and phase separation is guaranteed. It was however reported that the interface is not maintained sharp and the phases are not strictly immiscible [177–180]. The free-energy model is based on a free energy functional, which accounts for surface tension in a thermodynamically consistent manner. This model uses the total density and the density difference to distinguish the phases, whereas the two approaches mentioned before using the density of each phase as the model parameters. Several works based on this model report simulations of multiphase flows with a high density ratio, $\mathcal{O}(1000)$ [181,182]. Finally, the mean-field theory model relies on an index function to track the interface between the two phases. Molecular interaction forces are introduced to simulate interfacial dynamics, although they are smeared out on a much larger scale using a mean-field approximation [150]. Surface tension and phase separation are thus already incorporated in the model. The mean-field theory model is valid in the nearly incompressible limit and for nonideal gases. This method was applied also in the simulation of multiphase flows with high-density ratios [183].
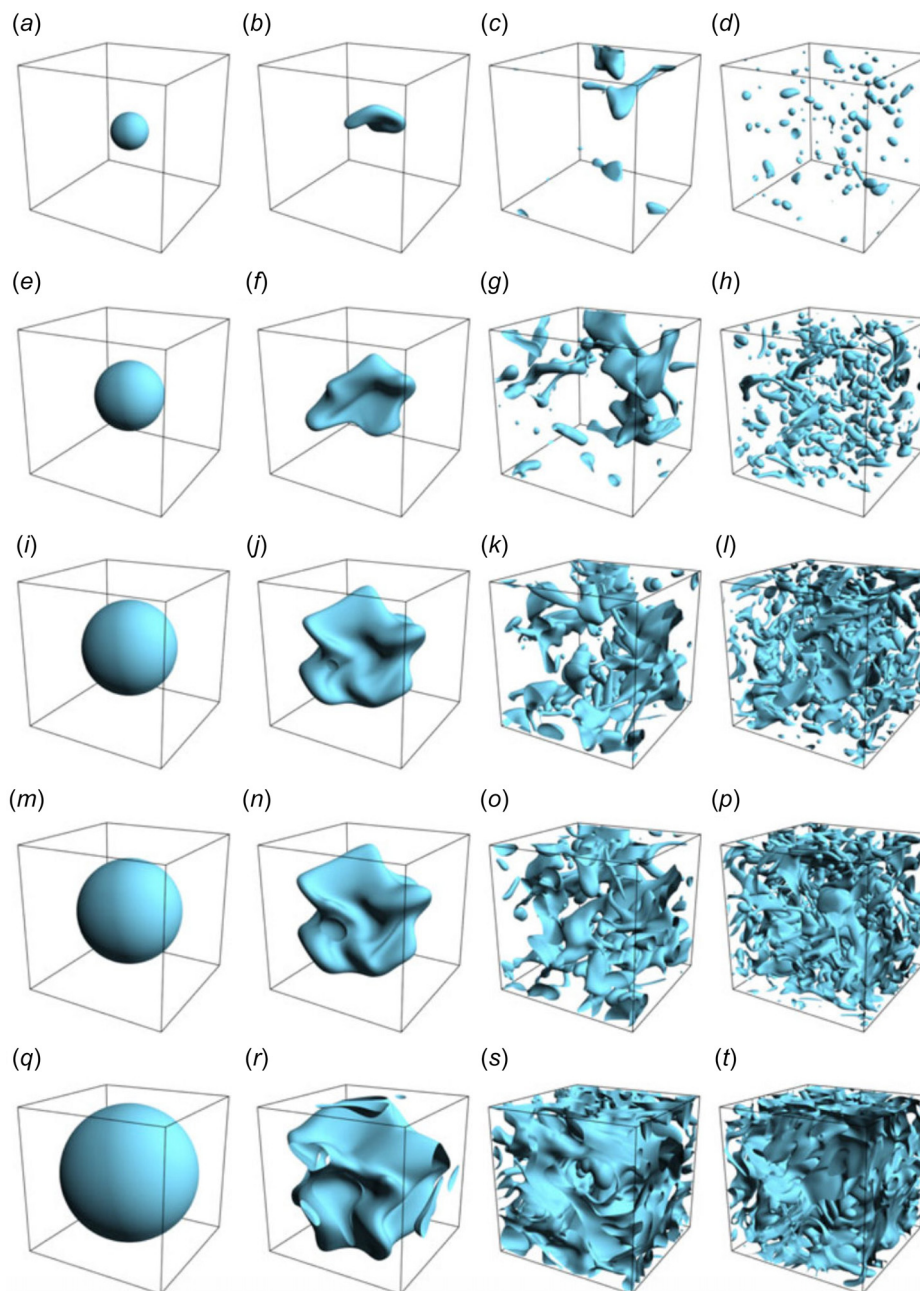
Fig. 8 Time-evolution of a spherical drop in forced homogeneous isotropic turbulence for different initial drop sizes (i.e., different volume fractions). The numerical simulation has been performed using a pseudo-potential lattice Boltzmann method. Adapted from Mukherjee et al. [153].

While LB approaches offer many advantages and have demonstrated their versatility, their use requires careful tackling of several issues. One of these is the strict restriction on the maximum time-step, which becomes extremely small as the flow Reynolds number is increased, making the simulations unfeasible or more cumbersome with respect to other methods in this limit. Indeed, as the Reynolds number is increased, the speed of sound has to be increased as well; the speed of sound in LB simulations is an artificial parameter (pseudo-compressibility) that allows for the solution to relax to the correct incompressible solution [163]. The speed of sound must be set in accordance with the low-Mach limit; for this reason, LB approaches cannot simulate real compressibility effects. In addition, the physical parameter (e.g., viscosity, density, surface tension, etc.) are not directly set in LB simulations, but their value is set via phenomenological parameters of the method (e.g., lattice spacing, time-step, relaxation time, sound speed, etc.) and by weighted integration of the particle distribution function. This specific characteristic limits the range of physical parameters that can be simulated to those for which the method is stable.

2.4 Surfactant Description. Surfactants are molecules that naturally collect at the interface between two fluids and locally modify the intermolecular cohesive forces among the fluid molecules, hence changing the surface tension value [184]. The presence of surfactants at the interface introduces complex interfacial dynamics: not only the magnitude of capillary forces is
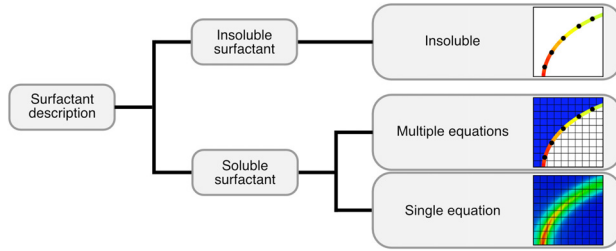
Fig. 9 Approaches commonly employed to describe the concentration of a surfactant. A first classification can be obtained considering the type of surfactant: soluble or insoluble. For insoluble surfactants, the methods commonly used rely on the solution of an advection-diffusion equation at the interface. For soluble surfactants, there are two possibilities: either coupling the insoluble surfactant method with an additional equation describing the surfactant dynamics in the bulk of the phases (multiple equation methods), either using a single surfactant concentration field in the entire domain (single equation methods).

reduced, but surfactant gradients along the interface also generate Marangoni forces [14], which act tangentially to the interface. Indeed, a clean (i.e., surfactant-free) interface feedback on the flow only through capillary forces (normal to the interface), whereas a surfactant–laden interface introduces additional forces (Marangoni forces, tangential to the interface), whose magnitude is proportional to the surface tension gradient, i.e., to the surfactant concentration gradient. This modification of both normal and tangential components of the surface tension forces may drastically change both local [15,184] and global [1–6,16] behavior of multiphase systems. Due to the key-role played by surfactants, the modeling and simulation of surfactant-laden flows received ever-increasing attention by the scientific community in the last 20 years. The choice of the numerical approach used to describe surfactants depends on the type of surfactant considered (nonionic, anionic, cationic, amphoteric, etc.), system configuration (liquid/liquid or gas/liquid), and fluid properties (polar or nonpolar, etc.). We can identify two main categories of surfactant behavior: soluble and insoluble surfactants [185]. Surfactants indeed do not dissolve in gases and their solubility in the liquid phase depends on the surfactant and liquid chemical properties [184,185]. Thus, based on the case considered, surfactant exhibits different dynamics: soluble surfactants can move along the interface and can transfer between the interface and the bulk of either phase (desorption and adsorption from/to the interface), while the dynamics of insoluble surfactants are limited only to the transport over the interface. In this latter case, the surfactant is actually insoluble (as hydrocarbon-based surfactants in water [185]) or has extremely low solubility so that it can practically be considered as insoluble. This different characteristic of surfactant is then reflected in the approaches used to track the surfactant concentration in numerical simulations: surfactant can be modeled as an insoluble species, present only at the interface, or as a soluble species, present at the interface and also in the bulk of the phases. From a numerical point of view, a further distinction can be made for this latter category: soluble surfactants can be described using a single equation or multiple equations coupled at the interface, thus separating interfacial and bulk dynamics. A schematic representation of the families of numerical approaches used to track the surfactant concentration is reported in Fig. 9.

2.4.1 Insoluble Surfactant Model

2.4.1.1 Methods for insoluble surfactants. These methods model the surfactant as an insoluble and nondiffusive species present solely at the interface between the two phases. The equation that describes the transport of surfactant over the interface [186] reads as
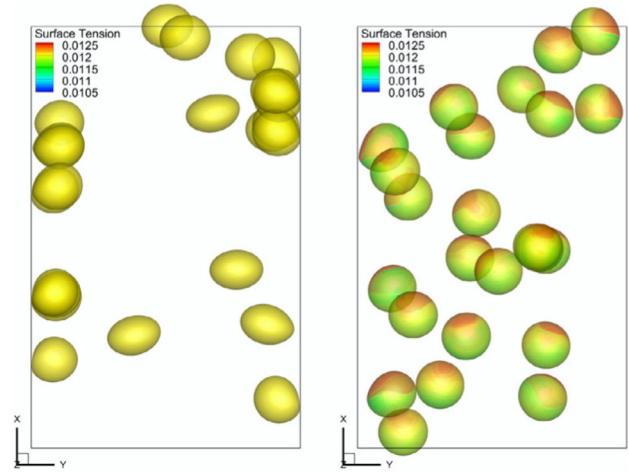

Fig. 10 Front Tracking simulation of a vertical channel flow laden with buoyant bubbles. The surface of the bubbles is covered with an insoluble surfactant: the bubble surface is colored using the local surface tension value. Here a standard Front Tracking scheme is adopted to track the bubbles, hence no topological modifications of the interface are allowed. Adapted from Lu et al. [190].

$$\frac{\partial \psi}{\partial t} + \nabla_s \cdot (\psi \mathbf{u}) + \psi (\nabla_s \cdot \mathbf{n})(\mathbf{u} \cdot \mathbf{n}) = D_s \nabla_s^2 \psi \qquad (11)$$

where $\nabla_s = (\mathcal{I} - \mathbf{n} \otimes \mathbf{n})$ is the surface gradient operator [187] ($\mathcal{I}$ is the identity matrix and $\mathbf{n}$ the unit-length vector normal to the interface) and D_s is the surface diffusion coefficient of the surfactant. The surfactant concentration ψ is defined only at the interface [115,188–191] or, for numerical reasons, in a narrow band about the interface [29,192–200]. The former approach is better suited for interface tracking methods, where the interface is explicitly defined with Lagrangian elements fitted to the interface, while the second approach is mostly used in combination with interface capturing approaches, in which the interface is not explicitly defined (Fig. 10).

2.4.2 Soluble Surfactant Model

2.4.2.1 Multiple equations methods. This class of methods, which can be considered an extension of the approaches used for insoluble surfactants, relies on the definition of different surfactant concentrations in the bulk (bulk surfactant concentration) and at the interface (interfacial surfactant concentration). Two (or more) transport equations are used to describe surfactant concentration in the subdomains (i.e., carrier phase, dispersed phase, and interface) and source/sink terms are used to couple the two separate systems (see the respective box in Fig. 9)

$$\begin{aligned} \frac{\partial \psi}{\partial t} + \nabla_s \cdot (\psi \mathbf{u}) + \psi (\nabla_s \cdot \mathbf{n})(\mathbf{u} \cdot \mathbf{n}) &= D_s \nabla_s^2 \psi + \dot{S}_\psi \\ \frac{\partial C}{\partial t} + \mathbf{u} \cdot \nabla C &= \nabla \cdot (D \nabla C) - \dot{S}_C \end{aligned} \qquad (12)$$

The first equation describes the surfactant transport on the interface, while the second one the surfactant transport in the bulk of the phases (D is the bulk diffusion coefficient of the surfactant); $\dot{S}_\psi$ and $\dot{S}_C$, are the coupling terms between the two separate domains. Similar to the formulations for insoluble surfactants, the surfactant concentration is defined at the interface [30,201–203] or in a thin layer across it [204,205]. When the interfacial surfactant concentration is defined only on a two-dimensional interface (e.g., using a front-tracking method), surfactant exchanges between the interface and the bulk occur in a thin adsorption layer adjacent to the interface [30,201–203]: the surfactant mass

adsorbed by the interface is distributed over the adsorption layer and then subtracted from the bulk concentration equation as a sink term. The source/sink term of the interfacial surfactant concentration transport consists of two terms, adsorption and a desorption contribution. The adsorption term describes the amount of surfactant that adsorbs from the bulk to the interface; it considers the bulk surfactant concentration at the interface, C_s, and the saturation interfacial surfactant concentration, ψ_∞, i.e., the maximum surfactant concentration allowed at the interface. The saturation interfacial surfactant concentration is the concentration corresponding to a monolayer of surfactant molecules over the interface [206]. Once a monolayer of surfactant is formed, no more surfactant molecules can collect at the interface; if further surfactant is added to the system, micelles, i.e., aggregates of surfactant molecules, will form in the bulk of the phases. It has been observed from experimental measurements on gas–liquid and liquid–liquid systems that the value of surface tension of a saturated interface corresponds to about half the surface tension value for the clean (surfactant-free) interface [206–209]. As an indirect consequence of the saturation dynamics at the interface, the surface tension value keeps constant once the interface has reached saturation conditions, which depend on the type of surfactant and mixture considered. The desorption term instead accounts for the surfactant that leaves the interface and dissolves into the bulk of the phases. The total flux of surfactant to the interface is thus

$$\dot{S}_\psi = k_a C_s (\psi_\infty - \psi) - k_d \psi \qquad (13)$$

where the adsorption and desorption coefficients, respectively, k_a and k_d, determine the magnitude of the adsorption and desorption fluxes. The source/sink term for the bulk surfactant concentration can be written as

$$\dot{S}_C = -D\mathcal{I}\mathbf{n} \cdot \nabla C|_{\text{int}} \qquad (14)$$

where $\mathcal{I}$ is an indicator function equal to one in the region occupied by the bulk fluid in which the surfactant dissolves and zero elsewhere, $\mathbf{n}$ is the normal to the interface and $C|_{\text{int}}$ is the bulk surfactant concentration evaluated at the interface. This contribution can be viewed as a boundary condition for the bulk surfactant transport equation [30,202].

From a numerical standpoint, first the source/sink term for the interfacial surfactant concentration transport equation, $\dot{S}_\psi$, is computed; then, this flux is redistributed over a thin adsorption layer adjacent to the interface (see the scheme in Fig. 11) in order to compute the source/sink term for the bulk surfactant concentration transport equation, $\dot{S}_C$

$$\dot{S}_{C_{i,j,k}} = -\sum_e \omega_{i,j,k}^e \dot{S}_\psi^e \frac{A^e}{V_{i,j,k}} \qquad (15)$$

Here i, j, k are the indices of the computational cell in the thin adsorption layer and e is the index of the surface element of the interface; $\omega_{i,j,k}^e$ is the corresponding weight, $V_{i,j,k}$ the volume of the computational cell (i, j, k), and A^e the area of the surface element e. The weights for each computational cell and surface element can be computed as

$$\omega_{i,j,k}^e = \frac{\tilde{\omega}_{i,j,k}^e}{\sum_i \sum_j \sum_k \tilde{\omega}_{i,j,k}^e} \qquad (16)$$

From the definition above it is straightforward to prove that $\sum_i \sum_j \sum_k \omega_{i,j,k}^e = 1$. The non-normalized weights, $\tilde{\omega}_{i,j,k}^e$, are defined as

$$\tilde{\omega}_{i,j,k}^e = \mathcal{D}(x^e - i\Delta)\mathcal{D}(y^e - j\Delta)\mathcal{D}(z^e - k\Delta) \qquad (17)$$
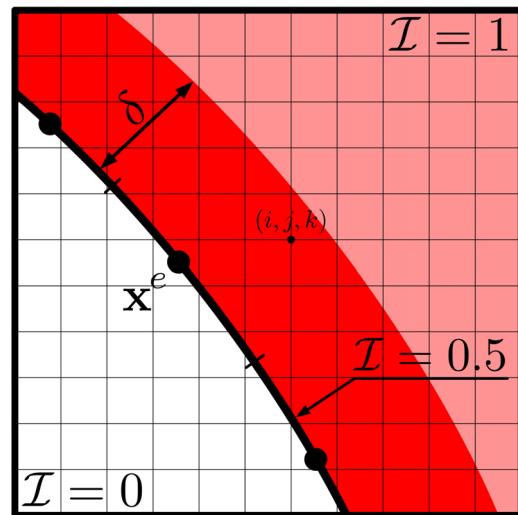
Fig. 11 Schematic of the redistribution of fluxes from the interface (solid black line, $\mathcal{I} = 0.5$) and the bulk region (light red and dark red regions, $\mathcal{I} = 1$). The thin adsorption layer (thickness δ) is reported in dark red and the computational grid is reported in the background with thin solid lines (grid spacing Δ). The sink/source contribution at the interface, $\dot{S}_\psi$, is computed at each surface element center, with coordinates $\mathbf{x}^e$, and then redistributed on the nearby nodes in the adsorption layer, denoted by the grid indexes (i, j, k). The sink/source contribution in the bulk, $\dot{S}_C$, is then computed in the adsorption layer. (See color figure online).

with (x^e, y^e, z^e) being the center of the surface element and Δ the grid spacing, assumed to be uniform in the three spatial directions. The smoothing kernel $\mathcal{D}$ is used to keep the exchanges of surfactant limited to the thin adsorption layer adjacent to the interface. The smoothing kernel is indeed nonzero only within the adsorption layer and in the phase where the surfactant dissolves (corresponding here to $\mathcal{I} = 1$)

$$\mathcal{D}(x) = \begin{cases} \dfrac{1}{\delta}\left(1 + \cos\dfrac{\pi x}{\delta}\right) & \text{if } |x| < \delta \text{ and } \mathcal{I} \geq 0.5 \\ 0 & \text{otherwise} \end{cases} \qquad (18)$$

It was shown that results are not particularly sensitive to the thickness of the thin adsorption layer δ (dark red region in Fig. 11) [30].

These formulations are particularly suited for gas–liquid systems, in which surfactant can dissolve in the liquid phase but is insoluble in the gas phase. These approaches can be used for liquid–liquid interfaces as well, by defining suitable surfactant transport equations in each phase: a separate surfactant transport equation can be defined in each subdomain (at the interface and in each phase). Since the surfactant subdomains are decoupled and a separate transport equation is defined for each of them, exchanges of surfactant (adsorption and desorption phenomena) have to be modeled.

2.4.2.2 Single equation methods. These approaches use a single concentration variable for the surfactant in the entire domain [28,152,210–212]. Thus, there is no separation between interfacial and bulk surfactant concentration. The evolution of the surfactant concentration variable, ψ, defined in the entire computational domain, is obtained by solving the equation (Fig. 12)

$$\frac{\partial \psi}{\partial t} + \mathbf{u} \cdot \nabla \psi = \nabla \cdot \left(\mathcal{M}_\psi \nabla \mu_\psi\right) \qquad (19)$$

where $\mu_\psi = \delta\mathcal{F}/\delta\psi$ is the surfactant chemical potential and $\mathcal{M}_\psi$ is the surfactant mobility. In analogy to the phase-field chemical potential, the surfactant chemical potential is obtained from free
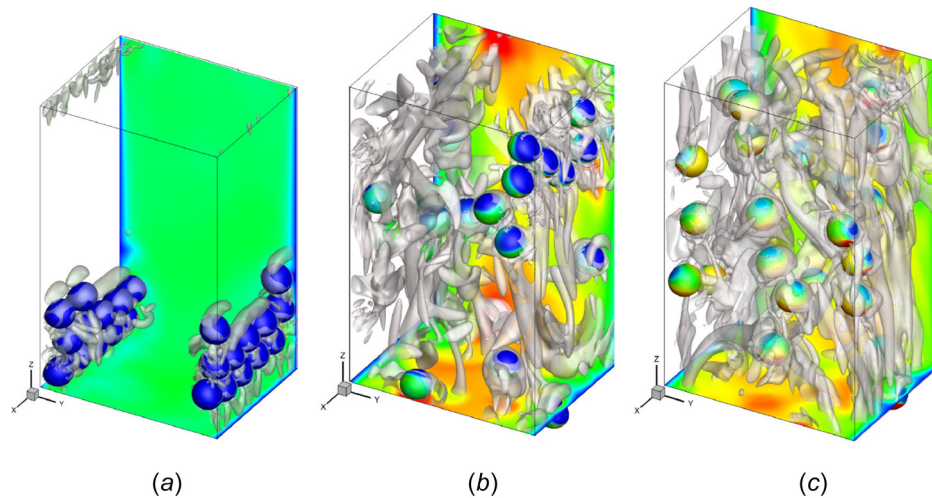
Fig. 12 Front Tracking simulation of a vertical channel flow laden with buoyant bubbles. A multiple-equation formulation is adopted to track the soluble surfactant separately in the bulk of the domain and over the interface. The interface of the bubbles is colored by the local surfactant concentration (blue—low, red—high); vortical structures (gray semitransparent surfaces) are displayed using the Q-criterion. Adapted from Ahmed et al. [203]. (See color figure online).

energy functional. Considering the simplest approach, three further terms are included in the phase-field functional, in addition to the terms of the classic Cahn–Hilliard formulation, controlling the interfacial behavior f_0 and f_{mix}

$$\mathcal{F} = \int_{\Omega} (f_0 + f_{mix} + f_\psi + f_1 + f_b)\mathrm{d}\Omega \qquad (20)$$

The first term, f_ψ, controls the surfactant diffusion and describes the entropy decrease obtained when the surfactant uniformly distributes in the entire domain; the second term, f_1, describes the surfactant adsorption and favors the collection of surfactant molecules at the interface. Finally, the last contribution, f_b, controls the solubility of the surfactant in the bulk of the two phases and thus describes the surfactant desorption from the bulk. Further terms can be included in the functional so to consider more complex surfactant dynamics [210]. Within this approach, surfactant accumulates at the interface and its concentration smoothly reduces to the bulk concentration within a thin transition layer about the interface (see the respective box in Fig. 9). This formulation is particularly suited for phase-field methods, as the surfactant physics can be directly included in the free energy functional governing the interfacial dynamics [210,211,213]. This way, surfactant accumulation at the interface and adsorption and desorption phenomena are already included in the formulation without the need for further models. Within this formulation, the surfactant concentration is defined as a volumetric concentration in a thin layer about the interface. These formulations are best suited to simulate liquid–liquid systems, in which the surfactant dissolves in both phases, even in the case of phases with different solubilities [214] (Fig. 13, [215]).

3   Challenges in the Simulation of Multiphase Turbulent Flows

The multiscale nature of multiphase turbulence imposes several challenges in the development and use of the simulation methods presented above. In particular, the challenge of simulating each and every time and length scale has to face the limitations of computing power and available memory [50]. Nowadays high-performance computing infrastructures can handle grids of the order of about 10^{10} points, while a hypothetical three-dimensional simulation of all scales, from the molecular scale of the interface
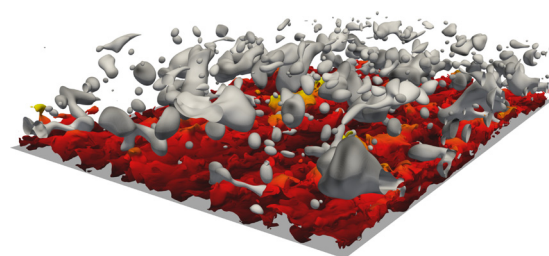

Fig. 13 Phase-field simulation of a swarm of drops laden with a soluble surfactant. The surfactant, reported on a grayscale colormap over the interface of the drops (white—low surfactant concentration, black—high surfactant concentration), is simulated using a single equation method. Flow structures are visualized using isocontours of the streamwise velocity, colored by their distance from the bottom wall (black—near wall, yellow—channel center). The presence of the surfactant reduces the surface tension at the interface according to the surfactant local concentration. The turbulent flow is thus able to strongly deform and break apart the drops. It can be appreciated how larger drops are concentrated at the channel center, where the shearing forces are weaker (and thus these droplets are stable), while smaller drops are more likely to be found close to the wall (bottom wall—gray plane and top wall—not shown) where the shearing forces are higher. Adapted from Soligo et al. [215]. (See color figure online).

to the macroscale of the flow, would require a cartesian grid with about 10^{27} points (about 10^9 grid points in each direction). In addition, small-scale physics becomes relevant as length scales become smaller and smaller: the continuum hypothesis breaks down and molecular-scale dynamics have to be taken into account [22,36,216]. The usual choice when interface-resolved simulation methods are employed (see Fig. 2) is to avoid resolving the small interfacial scales and to resolve all turbulence scales: from the macroscopic problem scale, down to the Kolmogorov length scale. In this way, however, all phenomena occurring at scales smaller than this threshold are modeled or somehow smeared out. This choice has direct consequences on the description of coalescence and breakage events and in the modeling of drops of size comparable to the grid spacing, which will be referred to as droplets. In the following, to assess the effects of modeling the smaller interfacial scales, the different stages composing a coalescence

and a breakage event will be detailed in Secs. 3.1 and 3.2, respectively. This description will be the starting point to assess the reliability of the numerical prediction of coalescence and breakage events. Finally, the issues concerning the simulation of droplets, i.e., drops of size comparable to the grid spacing, are presented: the lack of sufficient numerical resolution affects the computation of the shape of the droplets and surface tension forces. Different strategies to address these issues are reviewed in Sec. 3.3.

3.1 Coalescence. The dynamics of a coalescence event can be divided into four stages [18]: (i) approach, the two drops come closer and closer and a thin liquid film is formed in between; (ii) film drainage, the thin liquid film between the drops starts to drain; (iii) film rupture, small–scale interactions lead to the rupture of the thin liquid film and the formation of a coalescence bridge; and (iv) reshaping, surface tension forces reshape the drop. Of these stages, film drainage and film rupture are governed by physical phenomena occurring at very small scales. In particular, during the final part of the film drainage, the thickness of the thin liquid film is about 10–100 nanometers [18,217]. Likewise, during film rupture, although a fundamental understanding of this stage is still lacking [18,218], the main driving mechanisms are often assumed to be related to small–scale interactions as van der Waals attraction forces [219], thermal and capillary fluctuations [37,220,221] and overlap of diffusive interfacial layers [222]. The accurate simulation of these phenomena is highly desirable for determining the final outcome of the collision event: the interfaces might merge, leading to drop coalescence, or bounce off and separate. Unfortunately, such simulation is not possible and, while the numerical description of the approach and reshaping stages can possibly be accurate (Figs. 14(b)–14(d)), the simulation of the film drainage and rupture stages is less accurate (Fig. 14(c)) and depends on the numerical method used. This issue, which is referred to as numerical coalescence, affects both interface tracking and interface capturing methods, though in different ways. For interface tracking methods, additional closure models (based, for instance, on the critical distance or on the contact time) are usually required to describe coalescence events [89,91,92]; the

outcome of the interface collision is thus governed by the choice of coalescence model and relative parameters. Differently, for interface capturing methods, coalescence is implicitly handled and two separate interfaces merge when they are closer than the grid spacing [152,223–225]. Thus, coalescence is influenced by the grid resolution and the coalescence efficiency is often overestimated: standard interface capturing methods have a unitary coalescence efficiency (i.e., all collisions result in a coalescence), while the actual measured coalescence efficiency is much lower [226,227].

To mitigate the issues introduced by numerical coalescence, we can identify two possible pathways [50,228]: the first involves the coupling of molecular simulations to continuum simulations, while the second relies on simple subgrid models which can handle the effects that are not completely resolved [229,230].

The first possibility, coupling of molecular dynamics simulations with continuum simulations, is in principle the most accurate and reliable solution. However, it is of difficult implementation: the physical mechanisms driving the rupture of the film are still unclear and are the object of ongoing investigations [18,37,42,218,219] and, thus, cannot be properly included in numerical simulations. Different mechanisms for the film rupture have been observed in molecular dynamics simulations, and they strongly depend on the models chosen [18,37,42,218–222]. An additional issue arises from the coupling of physics and equations which act at very different spatial (millimeters versus nanometers) and temporal (microseconds versus picoseconds) and is thus separated by six orders of magnitude. Finally, the two approaches rely on different formulations and assumptions (continuum versus discrete).

The second possible choice is based on the inclusion of subgrid models which try to mimic the unresolved small-scale physics. These models are based on the assumption that the film drainage follows a simple lubrication model [36,50,228], but rely on different assumptions. We can distinguish among three different approaches: analytic and semi-analytic models, macroscopic or phenomenological models, and collision models. Analytic and semi-analytic models consider that at small scales capillary forces and viscous terms dominate: the geometry of the interface is simpler (surface-tension-dominated) and the flow field is simpler as well (viscosity-dominated) [36,50,228]. These features justify the adoption of simplified models; although the small-scale dynamics are not resolved, these models provide a fair approximation of the actual dynamics and can improve the numerical description of the film drainage stage, the most crucial phase in determining whether drops will coalesce or bounce off. For these reasons, the adoption of analytic and semi-analytic models appears to be a promising option to improve the numerical simulation of coalescence events. To determine whether two colliding interfaces should merge, two different approaches are usually adopted, the first is based on the contact (or interaction) time [231], while the second is based on the minimum film thickness [232,233]. In the first case, interfaces are merged if the contact time exceeds the time required for a complete drainage of the liquid film; if the contact time is smaller, interfaces rebound before merging takes place. The second approach is based on the minimum thickness that can be reached by the liquid film: if the film thickness decreases below an arbitrarily set value, interfaces are merged. Regardless of the particular approach chosen (contact time or film thickness), in both cases the interfaces are artificially merged as soon as the criterion for interface coalescence is met. Some of these lubrication models account also for rarefied flow effects [231–234]: when the Knudsen number (ratio of the mean free path over a reference length scale, taken in this case as the film thickness) approaches unity, the continuum hypothesis breaks down and suitable corrections for the friction (slip models) have to be included [234]. Alternative to the use of lubrication models, a possible solution is to employ macroscopic models. Their general framework is based on a localized forcing [235–237], which is added at the interface in the collision region (i.e., where two separate interfaces are closer than a certain
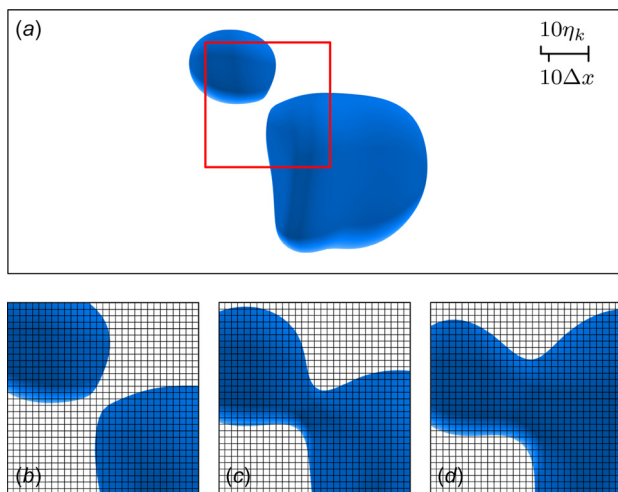

Fig. 14 Time sequence of a coalescence event, panels (b)–(d), top view. The event refers to the drops reported in panel (a). After the initial approach (panel b), the thin liquid film drains, a bridge is formed and the two drops merge (panel c); finally, surface tension forces reshape the newly formed drop (panel d). A red box (top row panel) identifies the region of the domain reported in the smaller panels (bottom row). The figure shows a top view of a turbulent channel flow laden with surfactant-laden droplets; adapted from Soligo et al. [152]. As a reference, the computational grid employed (which has a spacing $\Delta x/\eta_k = \Delta y/\eta_k \simeq 0.85$, with η_k being the Kolmogorov length scale) has been also reported. (See color figure online).

imposed threshold), thus repelling the interfaces. This repulsive force is a mesoscale representation of near-contact forces [236], which cannot be actually resolved as they act at a length scale much smaller than the resolved ones. It must be noted that none of these macroscopic models can possibly resolve the dynamics of the thin film in between the interfaces (even with a simplified approach), but they are instead phenomenological models aimed at reproducing the outcome of drop-drop collisions as observed in experiments and physical systems. Indeed, these phenomenological macroscopic models require ad hoc-tuned parameters, which cannot be easily traced back to physical principles.

Although oversimplified, there is a third possible solution to predict the outcome of drop–drop collision, which is based on a Weber number-impact parameter map [238,239]. From experimental measurements, different regimes (coalescence, bouncing, stretching, and reflexive separation) can be identified as a function of the Weber number and the impact parameter [240]; in the original formulation, only two regimes (coalescence and bouncing) were identified [238]. Based on the values of the Weber number and impact parameter, different outcomes for the drop–drop interactions can be predicted. Clearly, this approach requires extensive tuning and a large experimental database to trace the map of the various regimes, which can substantially differ according to the properties of the system considered.

3.2 Breakage. The dynamics of a breakage event can be divided into three stages [241,242]: (i) thread formation, the shear stresses stretch the drop and a ligament is formed; (ii) pinch-off, the thread elongates and capillary instabilities pinch-off the ligament (neck formation); and (iii) thread breaking, the liquid thread breaks at the pinch-off section and the newly formed drops separate. Upon separation, surface tension reshapes the drops and the threads are retracted. Overall, breakage is a very quick phenomenon that can be well approximated by the Navier–Stokes equations [152,243,244] without resolving the dynamics at the molecular scale. Therefore, regardless of the methodology used, the description of breakages using grids typical of interface-resolved methods is considered to be rather accurate [91,92,245], although in the pinch-off region the high curvature of the interface
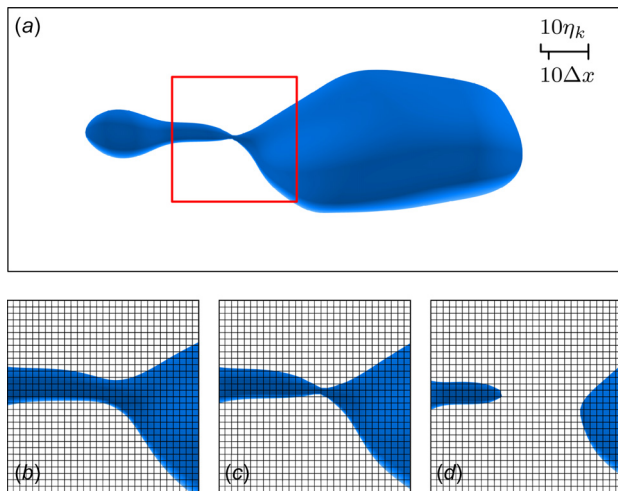

Fig. 15 Time sequence of a breakage event, panels (b)–(d), top view. The breakage refers to the drop reported in panel (a). The drop is stretched and a liquid thread is formed and thins (panels b), forms a neck (panel c), and subsequently breaks at the necking point (panel d). A red box (top row panel) identifies the region of the domain reported in the smaller panels (bottom row). The figure shows a top view of a turbulent channel flow laden with surfactant-laden droplets; adapted from Soligo et al. [152]. The computational grid employed (which has a spacing $\Delta x/\eta_k = \Delta y/\eta_k \simeq 0.85$, with η_k being the Kolmogorov length scale) has been also reported. (See color figure online).

may not be perfectly resolved. Breakage events are implicitly described in interface capturing methods [116,129,138], while interface tracking methods require suitable algorithms to manage the connectivity of the marker points [64,89]. An example of a numerical description of a breakage event is reported in Figs. 15(a)–15(d), which shows the different stages together with the computational grid and the length scale with respect to the Kolmogorov length scale; the event refers to the simulations reported in Soligo et al. [152].

While adaptive mesh refinement (AMR) offers only a partial improvement in the simulation of coalescence events [36,50,228], its use is largely beneficial in the description of thin filaments breaking, such as those observed when a drop is sheared and broken apart. In particular, AMR can be used to improve the description of the pinch-off region, which is characterized by high curvature values and thus high surface tension forces. For these reasons, AMR finds application in the simulation of breakage-dominated phenomena, such as the primary atomization of a liquid jet embedded in a fast stream of gas [46,246]. Within this framework, the refined level-set grid [46,48,131,246] uses a secondary more refined grid in a narrow region about the interface; the level-set function, defining the instantaneous position of the interface, is discretized on this finer grid. The level-set transport is thus resolved on this auxiliary grid; closure models for laminar sub-Kolmogorov conditions are then introduced to compute the subgrid velocity field [48], which is then added to the velocity field computed on the coarse grid. This method resembles an LES or a RANS approach, due to the introduction of subgrid models for the velocity.

3.3 Small-Scale Droplets. An additional issue arising from the limited resolution that one can afford when performing numerical simulations (and from the consequent lower bound set on time and length scales) is the minimum size of the single dispersed-phase droplet or ligament that can be simulated with sufficient accuracy. This problem affects simulations characterized by low surface tension (i.e., high Weber number) or secondary atomization processes, in which the range of scales (from the large scale of the jet, down to the smallest droplets and ligaments generated in the breakage of the jet itself) exceeds those that can be covered by a numerical simulation. When the size of the droplet becomes comparable to the grid size (depending on the numerical approach chosen to describe the interface, the minimum grid requirements slightly change), the geometry of the interface is poorly defined, thus affecting curvature calculation and even mass conservation.
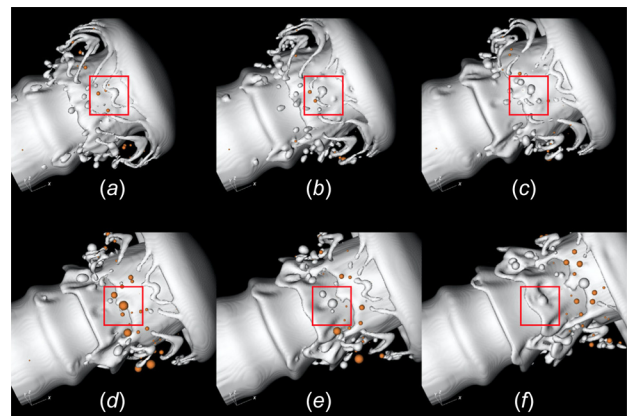

Fig. 16 Simulation of an atomization process performed using a hybrid Lagrangian–Eulerian formulation. The large–scale interfaces (white) are resolved using a VoF method while the smaller droplets (orange) are described using a LPT method. Adapted from Ling et al. [47]. (See color figure online).
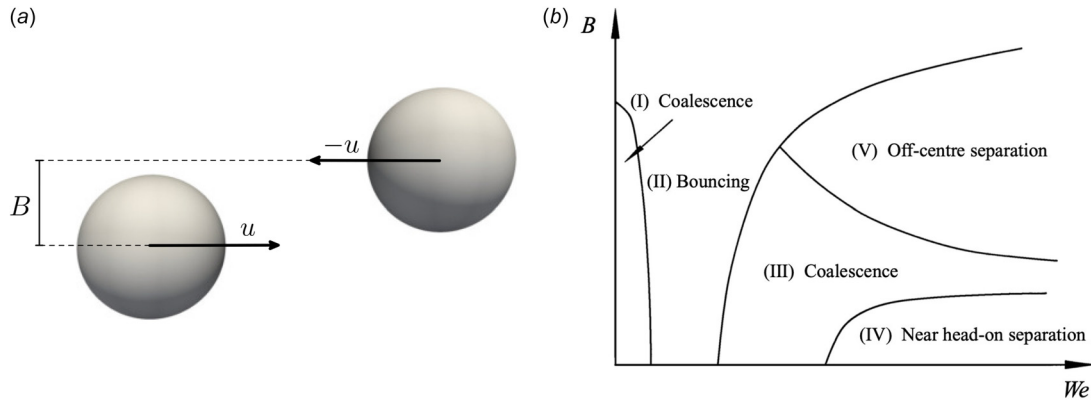
Fig. 17 Panel (*a*) shows a sketch of the setup considered to investigate the outcome of the drop-drop collision. Panel (*b*) shows the Weber-impact parameter diagram obtained from experimental measurements of the collision outcome of hydrocarbon droplets in the air (adapted from Qian and Law [260]). Different collision outcomes can be obtained for different combinations of the parameters: (I)-(III) coalescence, (II) bouncing, (IV) near head-on, and (V) offcenter separation.

A possible workaround to this issue is the adoption of hybrid Lagrangian–Eulerian formulations [40,46,47,246–249] (Fig. 16): the dispersed phase is described using an Eulerian approach (e.g., the volume of fluid or level set) as long as the size of the drop is larger than a set threshold (usually, about few grid cells), while smaller droplets are described as Lagrangian pointwise particles. More precisely, when a droplet is smaller than the threshold size (e.g., after a breakage) and has an aspect ratio close to unity (i.e., it is a droplet, not a ligament), it is transferred from the Eulerian field to the Lagrangian tracker; mass and momentum are preserved in the transfer. To keep into account eventual coalescence events, the droplet can be moved back from the Lagrangian tracker to the Eulerian field when it approaches an Eulerian interface. Clearly, when transferring drops from a finite-size Eulerian to a pointwise Lagrangian description, suitable filtering and adaptation of the flow field in the surrounding of the droplet itself have to be applied [47]. In the framework of hybrid Lagrangian–Eulerian schemes, surface tension forces are dominant, hence the shape of subgrid droplets can be safely assumed to be spherical [250]. This assumption may also be removed and models can be adopted to describe the deformation of these subgrid droplets. These models, relying on the phenomenological equation developed by Maffettone and Minale [251] to describe the droplet deformation tensor, have recently been applied to a different type of flows to describe the deformation of sub-Kolmogorov droplets [252–254] and bubbles [255].

4 Drop Size Distribution and Advancements

An accurate prediction of mass, momentum, and heat transfers through a fluid–fluid interface is crucial in many engineering applications and nature [1–6,256]. These transfers depend on mainly two parameters: the transfer rate and the total interfacial area. The former can be estimated using models or experimental correlations, while the latter can be computed from the drop size distribution (DSD). The DSD, differently from the average drop size, gives a broader information on the morphology of the dispersed phase, as it quantifies the number density of drops for each size, making thus possible to better estimate the total interfacial area. When a dispersed phase interacts with turbulence, a wide spectrum of drop sizes is generated: drops are broken apart by turbulent eddies, collide and eventually coalesce.

It has been observed that larger drops are more likely to break into smaller drops, while smaller drops are less likely to be broken apart and coalesce more frequently. Whether a drop break is determined by the balance of shearing forces (acting to break the drop) and surface tension forces (minimizing the total surface area, thus

hindering drop breakage). Starting from this balance, the maximum size of a drop that will resist breakage can be determined; this size is commonly identified as Hinze diameter, d_H [257]

$$d_H = 0.725 \left(\frac{\rho}{\sigma}\right)^{-3/5} \varepsilon^{-2/5} \qquad (21)$$

where ρ is the density of the carrier phase, σ the surface tension, and ε the fluid turbulent dissipation rate. A reference value for the dissipation is commonly assumed when computing the Hinze diameter; however, due to turbulence intermittency and to variations in the local dissipation (i.e., presence of turbulent eddies with different sizes and energy contents), the Hinze diameter does not mark a sharp threshold [258] and is instead a reference scale separating two regimes, the coalescence-dominated regime, for drops smaller than the Hinze scale, and the breakage-dominated regime, for drops larger than the Hinze scale. The physical mechanisms generating the DSD are complex and hard to disentangle; however, broadly speaking the DSD can be considered as the ultimate result of drop–drop and drop–turbulence interactions, namely, coalescence and breakage events.

The dynamics of these events, which change the topology of the interface, are rather challenging to capture with numerical simulations [33,152,228,259]. To investigate how much of the real physics can be captured with numerical simulations, we focus on coalescence events, as their numerical description is the most challenging, and we consider a rather simple setup: the collision and eventual coalescence of two drops in laminar flow. In this simple setup, two drops are brought into collision, as reported in Fig. 17(*a*). The two main parameters governing the problem are the Weber number, We, the ratio between inertia and surface tension forces, and the impact parameter, *B*. The impact parameter is the projection in the drop velocity direction of the distance between the center of the drops; for zero impact parameter, a head-on collision will occur, while for larger impact parameters an off-center collision will take place. Figure 17(*b*) shows the collision outcome as a function of the Weber number and the impact parameter for liquid drops in the air. Five different regimes can be identified: (I) coalescence (small deformation), (II) bouncing, (III) coalescence (high deformation), (IV) near head-on separation, and (V) offcenter separation [260]. At low impact parameters and low Weber numbers the drops slowly approach each other and successively coalesce (regime I, coalescence): as the drops are slowly approaching, the gas film in between the drops drains without opposing much resistance to the drainage. Once the distance between the approaching interfaces is small enough, short-range molecular forces draw the interfaces even closer till they merge.
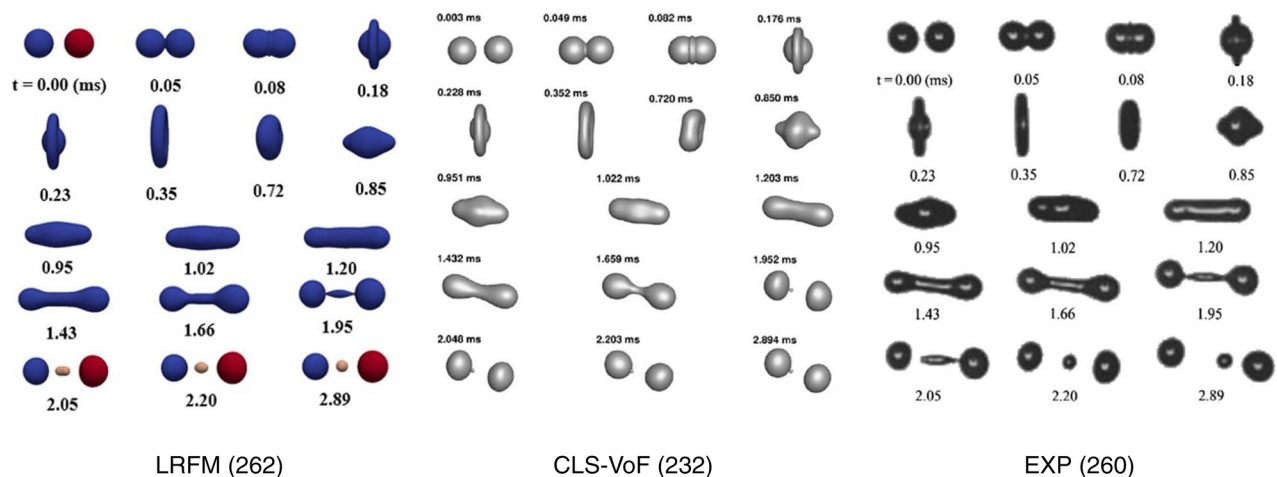
Fig. 18 Visual comparison among the simulations performed by Rajkotwala et al. [261] (left column, LRFM, local front reconstruction method) and Kwakkel et al. [231] (central column, CLS-VoF) and the experiments of Qian and Law [260] (right column, experiments — EXP) for drop-drop collisions in the near head-on separation regime (regime IV). Time is reported in milliseconds. In this regime, after the initial merging of the two drops ($t = 0.08$ ms), an outward spreading disk is formed ($t = 0.35$ ms); under the action of surface tension forces, this disk contracts and the drop stretches out along the collision axis forming a dumbbell ($t = 1.35$ ms). The large impingement inertia leads to the breakage of the ligament ($t = 1.95$ ms) and drops separate; smaller satellite droplets may be formed during the retraction of the ligament. In the left column the different marker functions (i.e., the different linked list of points) are reported using different colors; as the drops merge and break the linked lists of points are updated. The simulations have been performed using models for the film drainage and film rupture stages. Adapted from Rajkotwala et al. [261]. (See color figure online).

As the Weber number is increased, the draining rate of the gas film increases as well; this leads to a pressure buildup in the gas film, which opposes the approaching of the two drops. If the interfaces are too far away for the short-range molecular forces to be dominant, the drops will bounce off, avoiding coalescence (regime II, bouncing); on the other hand, if the inertia of the drops (i.e., the Weber number) is high enough, it can overcome the resistance of the pressure buildup in the gas film, leading to coalescence (regime III, coalescence with high deformation). Further increasing the Weber number, we observe three different possible collision outcomes, depending on the value of the impact parameter. For small values of the impact parameter, the liquid drops initially merge; however, the large normal component of the impingement inertia leads to separation and eventually to the formation of smaller satellite droplets (regime IV, near head-on separation). A time series showing a head-on separation of two colliding drops can be appreciated in Fig. 18 (the first two panels are obtained from numerical simulations [231,261], while the third from experimental measurements [260]). For intermediate values of the impact parameter, the smaller normal component of the impingement inertia reduces the internal flow responsible for the separation [260] and permanent coalescence is obtained (regime III, coalescence with high deformation). Finally, for larger values of the impact parameter, after the initial merging of the two drops, the rotation (and the induced centrifugal forces) causes the breakage of the newly formed drop (regime V, offcenter separation). Overall, Fig. 17(*b*) allows us to distinguish among five different possible collision outcomes. Naturally, this diagram is not unique and different combinations of the liquid and gas properties (e.g., drop viscosity, type of liquids, ambient gas pressure, etc.) lead to different collision maps [226,262–266].

To reproduce the different possible outcomes in simulations, an accurate description of the draining of the thin film is necessary [267]. Indeed, the draining of the thin film is crucial in determining whether the interfaces will get close enough for short-range molecular forces to be dominant, eventually leading to coalescence. In most cases, the dynamics of the thin film cannot be resolved exactly with numerical simulations, especially when the film thickness becomes of the order of the grid spacing or smaller. Then, depending on the numerical approach, the two interfaces may merge (as in classic interface capturing methods) or rebound

(as in classic interface tracking methods), thus leading to the issue of numerical coalescence. A possible workaround to the overestimated coalescence efficiency in interface capturing methods is the use of a multimarker approach, as done by Sussmann in a level-set framework [268]. This approach alone, while allowing to describe bouncing drop collisions, completely sorts out all coalescences: the different drops are treated as separate nonmiscible phases. A more refined solution is to couple the multimarker approach with a film drainage model [231,261,269]: the use of a multimarker approach prevents numerical coalescence, then, when the film thickness lowers below a certain threshold, a film drainage model is used to simulate the subgrid-scale flow in the thin film. The thin-film model accounts for the shape of the approaching interfaces, albeit in a simplified way, and for rarefied-flow effects (i.e., when the film thickness becomes comparable to the molecular mean free path) [231–234]. If the contact time between the drops is lower than the drainage time, the drops rebound (bouncing). On the other hand, if the drops are still at a close distance after the thin film is completely drained, the interfaces are merged (coalescence). The drops, which initially had different marker functions, merge in a single drop with its own marker function. A suitable algorithm manages all the marker functions: marker functions are merged whenever a coalescence occurs, while new ones are created upon breakage events [231]. A simplified version of the film drainage model assumes an arbitrarily chosen time to complete the drainage of the thin film and allows the drops to coalesce if their contact time is longer than this assumed drainage time [90,93]. Thus, instead of resolving the dynamics of the thin film, an adjustable parameter, the interface rupture time, is assumed. This latter model has been coupled with front tracking approaches, in which topological modifications of the interface (as, for instance, coalescences and breakages) have to be explicitly modeled.

Another possibility is to use a short-range repulsive force as a mesoscale representation of near-contact forces [235–237], as, for instance, van der Waals or electrostatic forces. The short-range repulsive force acts only in the close proximity of the interface, usually in a halo few grid cells thick surrounding the drop, and is only active in the area where halos belonging to different drops superpose, as shown in the scheme in Fig. 19. This latter model depends on relatively few parameters, namely, the thickness of
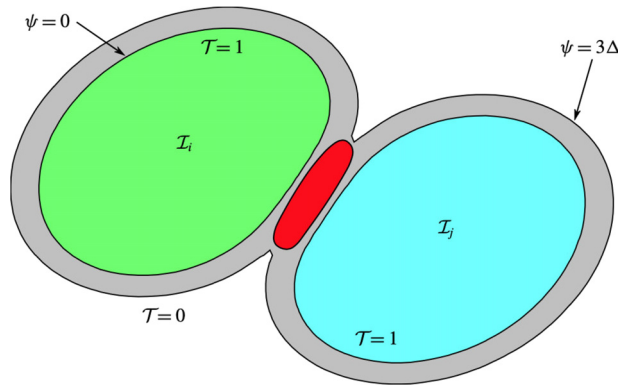
Fig. 19 Scheme of the algorithm used to impose a short-range repulsive force on two colliding drops. The two approaching drops (green and cyan, bounded by the interface $\psi = 0$) are identified by two separate markers $\mathcal{I}_i$, $\mathcal{I}_j$. Each drop has a surrounding halo (gray area); the forcing is applied on the region where halos belonging to different drops superpose, i.e., the red area. Adapted from De-Vita et al. [235]. (See color figure online).

the halo and the magnitude of the force. Overall, there is clearly a tradeoff between the model complexity and its physical background. Simpler models (as, for instance, the repulsive force or the imposed time-to-coalescence model) require very few arbitrary parameters to be set, but at the same time, they lack a strong physical background, as their aim is to approximate the molecular-scale phenomena on a much larger scale. Differently, more complex models (as, for instance, drainage models) require less arbitrary parameters, but use instead input data from the large-scale simulation (e.g., initial and boundary conditions) and then provide an output to the large-scale simulation (as, for instance, the time required to complete the drainage [231] or the pressure in the thin film [233]).

The use of these models in simulations of drop-drop collisions is beneficial: previous works where these models are employed were able to fairly reproduce the Weber number-impact parameter diagram [231,233,261]. In particular, although the critical Weber number (transition from bouncing to high-deformation coalescence) exhibits a grid resolution dependence [233], the different collision outcomes can be reproduced and the resulting collision map exhibits only a weak dependence on the grid resolution [231,261]. To visually appreciate this agreement, a comparison among two different simulations (respectively, those reported in Rajkotwala et al. [261] and Kwakkel et al. [231]) and the experiments of Qian and Law [260] is shown in Fig. 18. All collisions reported referring to regime IV, near head-on separation.

Extending the use of these models to turbulent flows laden with a large number of drops of different sizes that mutually interact is a rather challenging task. Indeed, in general, the use of these models requires an additional algorithm that detects drop-drop collisions. For the simpler coalescence models (repulsive force or contact time), this algorithm is used to determine whether a repulsive force needs to be applied or a timer measuring the contact time has to be started, while for more sophisticated approaches (e.g., film drainage), it is required to determine when an additional parallel simulation that computes the film drainage dynamics has to be started [231]. The computational cost of this algorithm is almost negligible for a small number of drops, while it drastically increases for a large swarm of drops or when large-scale simulations are performed. Hence, the use of coalescence models has mainly been limited to relatively simple cases (e.g., drop-drop collisions) with fewer cases involving multiple drops carried by a turbulent flow [91,92]. Lu and Tryggvason [91,92] included a coalescence model in their numerical simulations of a swarm of bubbles in a vertical channel flow to investigate the effect of coalescence. It must be noted however that, being a front-tracking-

based approach, topological modifications of the interface have to be explicitly defined as they are not already intrinsic to the interface tracking model; in these works, coalescence took place whenever the interfaces were closer than a certain arbitrary threshold. These works mainly focused on investigating the effects of the topological modifications of the interface (hence, of the proposed coalescence model) on the flow and did not provide any information on the simulated bubble size distribution, so the question of whether such coalescence model is able to recover the scaling observed for the coalescence-dominated regime is still open. An additional difficulty comes from the presence of small drops or bubbles, whose size is comparable to the grid resolution and hence will not be properly resolved on a relatively coarse grid (and as well their mutual interaction).

The difficulties in improving the description of coalescence events pose some limitations on the information that can be extracted from large-scale simulations, and in particular on the drop size distribution. In most of the cases, we expect that simulations will not be able to accurately describe the coalescence-dominated regime, i.e., the dynamics of drops smaller than the Hinze scale. These drops are unlikely to break apart in smaller droplets, and will more likely interact with the surrounding drops, thus stressing the limitations of the numerical description of coalescence events. In addition, a fraction of these drops have a size comparable to the grid size and, as a consequence, their numerical description is not particularly accurate. In the breakage-dominated regime, covering the dynamics of drops larger than the Hinze scale, we expect instead a rather accurate prediction: larger drops are very prone to be broken apart by turbulence and will interact less with the surrounding drops. This aspect strongly limits the impact of numerical coalescence on the results and instead leverages the fairly accurate description of the breakage events. Furthermore, the description of larger drops is more accurate than for smaller drops, as the grid spacing is much smaller than the drop size.

To confirm these speculations and to verify the quality of the numerical predictions, we compare the results obtained in previous works with analytic scalings and experimental data. For the analytic scalings, several models to predict the resulting DSD were proposed. Among these, the most commonly adopted distributions are: normal [270,271], log-normal [272–274], Rosin-Rammler [275], Weibull [276], upper limit equation [277], and power-law [278–283]. Although a universal agreement over several decades has not been yet demonstrated, several experimental [278,284,285] and numerical [152,153,279,281,282,286] works, in which turbulent flows laden with drops are considered, report a good agreement with a power-law scaling. In particular, for the coalescence-dominated regime (drops smaller than the Hinze scale), Deane and Stokes [278], using arguments from the mechanics of steady-state jets and considering the case of breaking waves, derived the following scaling:

$$P(d) \propto Q\left(\frac{\rho}{\sigma}\right)^{3/2} u^2 d^{-3/2} \qquad (22)$$

where Q is the volume of air (i.e., dispersed phase) entrained per volume of water (i.e., carrier phase) per second, ρ the carrier phase density, u a characteristic velocity and d the droplet diameter. For the breakage-dominated regime (drops larger than the Hinze scale), Garrett et al. [280], assuming a break-up cascade mechanism and considering the case of breaking waves, proposed the following scaling:

$$P(d) \propto Q\varepsilon^{-1/3} d^{-10/3} \qquad (23)$$

where ε is the fluid turbulent dissipation rate. Although the model proposed by Garrett et al. [280] relies on strong physical arguments and can be applied to different turbulent multiphase flow instances [283], a universal agreement on the value of
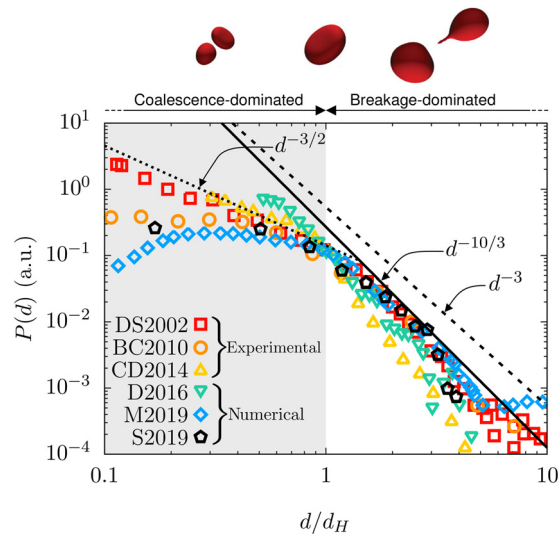
Fig. 20 Comparison of the drop size distribution computed using different numerical approaches and obtained from experimental measurements; the analytic scaling law for the coalescence-dominated regime (gray), $d^{-3/2}$, and the scaling laws for the breakage-dominated regime (white), $d^{-10/3}$ and d^{-3}, are also provided for reference. The data are adapted from Deane and Stokes (DS2002, experimental [278]), Blenkinsopp and Chaplin (BC2010, experimental [284]), Callaghan and Deane (CD2014, experimental [290]), Deike et al. (D2016, VoF [279]), Mukherjee et al. (M2019, LB [153]) and Soligo et al. (S2019, PF [152]). The drop diameter is normalized using the Hinze diameter for each case, while the drop size distribution is reported in arbitrary units due to the different normalizations adopted in the various works. A fair agreement is obtained in the breakage-dominated regime, i.e., for drops larger than the Hinze diameter.

the exponent (i.e., $\alpha = -10/3$) has not been obtained yet, and previous works reported values varying between $\alpha = -3$ [279,282,284,285,287] and $\alpha = -10/3$ [278,280,288,289]. In Fig. 20, the results obtained from previous numerical works, all of which employed different numerical methods (lattice Boltzmann [153], volume of fluid [279], and phase-field method [152]), are compared against the experimental data of Deane and Stokes [278], Blenkinsopp and Chaplin [284], and Callaghan and Deane [290]. The scalings for the coalescence-dominated regime (exponent $\alpha = -3/2$, dotted line) and the breakage-dominated regime (exponents $\alpha = -3$ and $\alpha = -10/3$, solid and dashed lines, respectively) are also reported as reference.

For the coalescence-dominated regime (gray region, drops smaller than the Hinze scale), considering the experimental results, only the data of Deane and Stokes [278] and Callaghan and Deane [290] seem to follow the $-3/2$ power law scaling, while the results of Blenkinsopp and Chaplin [284] deviate from the analytic scaling and the measured exponent is close to zero. It must be noted, however, that for the experimental dataset of Callaghan and Deane [290], only a few points below the Hinze diameter are available; thus the scaling exponent cannot be accurately quantified. This discrepancy observed among the experimental results [278,284,290] can be explained considering differences in the type of measurements (steady-state or transient) and the specifics of the experimental techniques adopted in each work. Likewise, considering the numerical results, which are obtained using different numerical methods (phase-field [152], lattice Boltzmann [153], and volume of fluid [279]), the difficulties in the simulation of coalescence phenomena, which are crucial in determining the drop size distribution below the Hinze diameter, negatively affect the accuracy of numerical simulations in this regime. Moving to the breakage-dominated regime (white region, drops larger than the Hinze scale), comparing experimental measurements [278,284,290] and numerical simulations [152,153,279] it can be

noticed how all methods accurately capture the scalings proposed for the breakage-dominated regime. Further data, spanning a wider range of scales, are however needed to identify the correct scaling exponent between $\alpha = -3$ and $\alpha = -10/3$. As of now, the limited range of sizes available does not allow us to infer the precise value of the exponent.

Overall, from the results reported in Fig. 20, it is clear how both experiments and numerical simulation struggle in capturing the proposed analytic scaling for the coalescence-dominated regime, while a much better agreement between experimental results, numerical results, and theoretical scaling laws can be achieved in the breakage-dominated regime. Improving the simulation of coalescence phenomena through simplified models or, by locally refining the computational grid in the region where the interfaces collide, would be of key importance to accurately simulate the dynamics of smaller drops, especially those smaller than the Hinze diameter and, thus to improve the results accuracy in the coalescence-dominated regime.

5 Conclusions

Turbulent multiphase flows play a key role in many natural phenomena and industrial processes. It is widely accepted that numerical simulations provide an invaluable tool to shed light on the intricate physics of these flowing systems, but it is also clear that the multiscale nature of these flows imposes computational requirements that cannot be matched by existing computational infrastructures: even with the help of cutting-edge high-performance computing infrastructures, only a fraction of the scales, which are crucial to determine the evolution of the system, can be directly resolved. Indeed, the typical range of length scales in multiphase turbulence covers about eight to nine orders of magnitude—from the interface description to the large-scale geometry, while current limitations of numerical simulations narrow this range to three—at most four—orders of magnitude. Several methods have been developed to simulate multiphase turbulent flows, and in this review, we focus on methods belonging to the interface-resolved family: all turbulent scales, from the scale of the largest flow structure down to the Kolmogorov length scale of the smallest eddies, are resolved, while smaller scales, including the molecular scale of the interface, are modeled or not resolved. This approach introduces inevitable inaccuracies in the simulations: phenomena acting at these scales are smeared out on the smallest resolved length scale. However, since phenomena occurring at the unresolved smaller scales are capable of influencing the physics at the larger scales, approximations introduced at the unresolved scales affect also the dynamics of the entire system. By far, the largest inaccuracy in the prediction of the multiphase system occurs when the dispersed flow undergoes topological changes, which is to say when two drops merge in a coalescence event or when one drop breaks into smaller drops during a breakage event. In particular, the impossibility of resolving the molecular-scale dynamics has a strong effect on the simulation of interface merging and breakage, for which the effects of the molecular-scale physics cannot be completely ruled out. The unfeasibility of performing numerical simulations that resolve all the scales mandates the use of additional models and suitable strategies. These models, however, do not resolve the missing physics and are rather an attempt to integrate the effects of these missing physics in the numerical simulation. For example, models that aim at improving the simulation of interface merging (i.e., coalescence) do not involve any of the molecular-scale physics that govern the rupture of the interface and the formation of the coalescence bridge; they provide instead a comparable effect albeit at a mesoscopic scale. Similarly, strategies such as the adoption of an AMR scheme have certainly their merit in the improvement of the simulation of interface breakage, however, the lower threshold on the smallest interfacial features that can be simulated is only shifted toward slightly smaller scales. Another issue, which is related to the simulation of the smaller interfacial

SUMMARY POINTS

1 Multiphase turbulence is governed by a physics acting over a wide range of scales: from the largest problem scale, down to the Kolmogorov scale of turbulence and further down to the molecular scale of the interface. This makes direct numerical simulations unfeasible and only a limited range of scales can be resolved.

2 Numerical capture of breakage events is not much influenced by the resolution: breakages are point-wise and quick events, which do not affect the overall flow dynamics. In addition, small scales physics do not play a significative role in the dynamics of interface breaking.

3 Numerical capture of coalescence events is influenced by the inevitable lack of resolution: the physics governing interface coalescence act at the molecular level and cannot be directly resolved with standard methods.

4 The description of small droplets and thin ligaments is influenced by the grid resolution: small-scale features of the interface (smaller than the grid size) cannot be captured.

5 Numerical simulations are an essential tool to investigate multiphase turbulence. Despite some issues, the drop size distribution predicted by numerical simulations in the breakage-dominated regime exhibits the same power law scaling obtained from theories and experiments.

Fig. 21   Summary points at a glance

FUTURE PERSPECTIVES

1 The use of models greatly improves the simulation of interface merging (coalescence). Although the exact mechanisms leading to the rupture of the film separating the coalescing interfaces are still under investigation, models can provide an improved description of small-scale interface-interface interactions.

2 Numerical simulations capture fairly well interface breakage. Adaptive mesh refinement can be used to capture with higher accuracy the shape of the liquid thread and the large curvature of the interface at the necking point.

3 Grid resolution establishes the limit of the smallest interfacial structures that can be resolved. Adaptive mesh refinement and hybrid Lagrangian-Eulerian approaches can be used to improve the description of small droplets and thin ligaments.

4 The increased complexity of the simulations, the larger computational cost and the potential arbitrariness of models are the main limiting factors to the use of approaches to model small-scale dynamics in large-scale simulations.

5 Numerical coalescence and lack of accuracy in the simulation of the smallest features of the interfacial phenomena are the most critical issues that next-generation numerical simulations need to address so that the full spectrum of the drop size distribution, coalescence- and breakage-dominated regimes, can be accurately captured.

Fig. 22   Future perspectives at a glance

features (although at a scale much larger than the molecular one), is the description of drops and ligaments whose size is comparable or smaller than the local grid resolution. In these cases, AMR strategies are rather successful, even though the intrinsic limitation on the smallest resolved scale is not removed, but it is just shifted toward smaller scales. The adoption of a hybrid Lagrangian–Eulerian formulation somehow removes this limitation on the smaller droplets, which are treated as pointwise particles and tracked within a Lagrangian framework, at the cost of losing the subgrid interfacial dynamics, which are only captured through simplified models. While there is no limitation on the smallest droplet size, a Lagrangian description of the droplets introduces some inaccuracies when moving the droplets between the Eulerian and the Lagrangian framework: the flow field must be adapted when adding or removing droplets from the Eulerian framework and the droplet shape is assumed a priori when inserting droplets from the Lagrangian framework back into the Eulerian one (Fig. 21).

Despite these issues, interface resolved simulations can still tell us plenty of information about the physics of the system. The comparison of the drop size distributions obtained from numerical simulations with experimental data [278,284,290] and analytic scalings [278,280] proves the capability of the current methods: a good agreement can be observed for drops larger than the Hinze diameter, i.e., in the breakage-dominated regime, hinting that the dynamics of interface breaking are well captured with numerical simulations. Differently, considering the coalescence-dominated regime, i.e., drops smaller than the Hinze diameter, numerical simulations struggle in reproducing the available data, indicating that the effects of numerical coalescence and the limited grid resolution are dominant in this region of the drop size distribution. It must be noted that also experimental measurements do not exhibit a common agreement in the coalescence-dominated regime, mainly due to differences in spatial and temporal resolution and

measurement techniques. Overall, we can safely state that, while the dynamics of the larger interfacial scales is accurately captured by numerical simulations, that of the smaller interfacial scales is affected by the grid resolution and by the eventual adoption of specific subgrid-scale models (Fig. 22).

All these issues need to be addressed to improve the accuracy of numerical simulations of multiphase flows; however, some of them are not as critical. We can indeed sort them by priority: it is clear that improving the simulation of interface merging and the smaller droplets and ligaments is more crucial than resolving with higher accuracy the breakage of the interface, which is already quite accurate in standard implementations. Acting on the first two issues, interface merging and smaller droplets, through models or AMR strategies comes however at a cost: the free parameters of the various approaches need to be carefully selected. For coalescence models, the choice of the parameters modifies the drop-drop collision outcome: for instance, the magnitude of the repulsive forcing determines whether the interfaces will merge upon collision [235]. Furthermore, the grid resolution has a negligible effect in certain film drainage models [231,261], while it is more important in others [233]. For AMR, a suitable minimum cutoff length has to be chosen carefully, minding that excessively reducing the grid spacing is often un-necessary and unfeasible [50,228]. Likewise, for hybrid methods, a length scale setting a threshold between the Eulerian and the Lagrangian description has to be selected: a large value of the length scale threshold introduces a consistent approximation when describing these droplets in the Lagrangian framework, while a small value leads to a poor description of the interface shape in the Eulerian framework. In addition to these issues linked with the choice of model parameters, one has also to consider the substantial increase in algorithm complexity and computational cost. Indeed, for coalescence models and AMR, algorithms that identify all the forthcoming

merging and breakage of the interface are required. The scalable and efficient implementation of these algorithms in parallel architectures, like those commonly employed to perform large-scale simulations, is a challenging task: complex data structures and an augmented volume of data communication increases the computational cost of the simulations, limiting the use of these approaches to rather simple configurations. Clearly, models able to capture the subgrid interfacial dynamics are of crucial importance in the simulation of multiphase turbulence; robust and high-performing algorithms to improve the numerical simulation of coalescence, breakage and small droplets are indeed a highly desirable feature in next-generation interface-resolved simulations. At the same time, a better understanding of the physics governing interface merging is sought to guide the development of more physics-aware coalescence models.

References

[1] Jähne, B., and Haußecker, H., 1998, "Air-Water Gas Exchange," Annu. Rev. Fluid Mech., **30**(1), pp. 443–468.

[2] Pereira, R., Ashton, I., Sabbaghzadeh, B., Shutler, J., and Upstill-Goddard, R., 2018, "Reduced Air-Sea CO_2 Exchange in the Atlantic Ocean Due to Biological Surfactants," Nat. Geosci., **11**(7), pp. 492–496.

[3] Kralova, I., and Sjöblom, J., 2009, "Surfactants Used in Food Industry: A Review," J. Disper. Sci. Technol., **30**(9), pp. 1363–1383.

[4] Dickinson, E., 2010, "Food Emulsions and Foams: Stabilization by Particles," Curr. Opin. Colloid Interface Sci., **15**(1–2), pp. 40–49.

[5] Karsa, D. R., 1999, Industrial Applications of Surfactants IV, Woodhead Publishing, Cambridge, UK.

[6] Schramm, L. L., Stasiuk, E. N., and Marangoni, D. G., 2003, "Surfactants and Their Applications," Annu. Rep. Prog. Chem., Sect. C: Phys. Chem., **99**, pp. 3–48.

[7] Bourouiba, L., Dehandschoewercker, E., and Bush, J. W. M., 2014, "Violent Expiratory Events: On Coughing and Sneezing," J. Fluid Mech., **745**, pp. 537–563.

[8] Balachandar, S., Zaleski, S., Soldati, A., Ahmadi, G., and Bourouiba, L., 2020, "Host-to-Host Airborne Transmission as a Multiphase Flow Problem for Science-Based Social Distance Guidelines," Int. J. Multiphas. Flow, **132**, p. 103439.

[9] Rosti, M. E., Cavaiola, M., Olivieri, S., Seminara, A., and Mazzino, A., 2021, "Turbulence Dictates the Fate of Virus-Containing Liquid Droplets in Violent Expiratory Events," Phys. Rev. Res., **3**, p. 013091.

[10] Rosti, M. E., Olivieri, S., Cavaiola, M., Seminara, A., and Mazzino, A., 2020, "Fluid Dynamics of COVID-19 Airborne Infection Suggests Urgent Data for a Scientific Design of Social Distancing," Sci. Rep., **10**, p. 22426.

[11] Mittal, R., Ni, R., and Seo, J.-H., 2020, "The Flow Physics of COVID-19," J. Fluid Mech., **894**, p. F2.

[12] Bahl, P., Doolan, C., de Silva, C., Chughtai, A., Bourouiba, L., and MacIntyre, C. R., 2020, "Airborne or Droplet Precautions for Health Workers Treating COVID-19?," J. Infect. Dis., pp. 1–8.

[13] Chong, K. L., Ng, C. S., Hori, N., Yang, R., Verzicco, R., and Lohse, D., 2021, "Extended Lifetime of Respiratory Droplets in a Turbulent Vapor Puff and Its Implications on Airborne Disease Transmission," Phys. Rev. Lett., **126**(3), p. 034502.

[14] Scriven, L., and Sternling, C., 1960, "The Marangoni Effects," Nature, **187**(4733), pp. 186–188.

[15] Dai, B., and Leal, L., 2008, "The Mechanism of Surfactant Effects on Drop Coalescence," Phys. Fluids, **20**(4), pp. 1–13.

[16] Takagi, S., and Matsumoto, Y., 2011, "Surfactant Effects on Bubble Motion and Bubbly Flows," Annu. Rev. Fluid Mech., **43**(1), pp. 615–636.

[17] Vakarelski, I., Yang, F., Tian, Y., Li, E., Chan, D., and Thoroddsen, S., 2019, "Mobile-Surface Bubbles and Droplets Coalesce Faster but Bounce Stronger," Sci. Adv., **5**(10), p. eaaw4292.

[18] Kamp, J., Villwock, J., and Kraume, M., 2017, "Drop Coalescence in Technical Liquid/Liquid Applications: A Review on Experimental Techniques and Modeling Approaches," Rev. Chem. Eng., **33**(1), pp. 1–47.

[19] Reinecke, N., Petritsch, G., Schmitz, D., and Mewes, D., 1998, "Tomographic Measurement Techniques—Visualization of Multiphase Flows," Chem. Eng. Technol., **21**(1), pp. 7–18.

[20] Lindken, R., Gui, L., and Merzkirch, W., 1999, "Velocity Measurements in Multiphase Flow by Means of Particle Image Velocimetry," Chem. Eng. Technol., **22**(3), pp. 202–206.

[21] Lindken, R., and Merzkirch, W., 2002, "A Novel PIV Technique for Measurements in Multiphase Flows and Its Application to Two-Phase Bubbly Flows," Exp. Fluids, **33**(6), pp. 814–825.

[22] Scardovelli, R., and Zaleski, S., 1999, "Direct Numerical Simulation of Free-Surface and Interfacial Flow," Annu. Rev. Fluid Mech., **31**(1), pp. 567–603.

[23] Prosperetti, A., and Tryggvason, G., 2009, Computational Methods for Multiphase Flow, Cambridge Press, Cambridge, UK.

[24] Elghobashi, S., 2019, "Direct Numerical Simulation of Turbulent Flows Laden With Droplets or Bubbles," Annu. Rev. Fluid Mech., **51**(1), pp. 217–244.

[25] Bull, J. L., Nelson, L. K., Walsh, J. T., Glucksberg, M. R., Schürch, S., and Grotberg, J. B., 1999, "Surfactant-Spreading and Surface-Compression Disturbance on a Thin Viscous Film," ASME J. Biomech. Eng., **121**(1), pp. 89–98.

[26] Dussaud, A. D., Matar, O. K., and Troian, S. M., 2005, "Spreading Characteristics of an Insoluble Surfactant Film on a Thin Liquid Layer: Comparison Between Theory and Experiment," J. Fluid Mech., **544**(1), pp. 23–51.

[27] Adami, S., Hu, X., and Adams, N., 2010, "A Conservative SPH Method for Surfactant Dynamics," J. Comput. Phys., **229**(5), pp. 1909–1926.

[28] Soligo, G., Roccon, A., and Soldati, A., 2019, "Coalescence of Surfactant-Laden Drops by Phase Field Method," J. Comput. Phys., **376**, pp. 1292–1311.

[29] Xu, J., Li, Z., Lowengrub, J., and Zhao, H., 2006, "A Level-Set Method for Interfacial Flows With Surfactant," J. Comput. Phys., **212**(2), pp. 590–616.

[30] Muradoglu, M., and Tryggvason, G., 2008, "A Front-Tracking Method for Computation of Interfacial Flows With Soluble Surfactants," J. Comput. Phys., **227**(4), pp. 2238–2262.

[31] Harlow, F. H., and Welch, J. E., 1965, "Numerical Calculation of Time-Dependent Viscous Incompressible Flow of Fluid With Free Surface," Phys. Fluids, **8**(12), pp. 2182–2189.

[32] Mirjalili, S., Jain, S., and Dodd, M., 2017, "Interface-Capturing Methods for Two-Phase Flows: An Overview and Recent Developments," Cent. Turbul. Res. Annu. Res. Briefs, pp. 117–135.

[33] Gorokhovski, M., and Herrmann, M., 2008, "Modeling Primary Atomization," Annu. Rev. Fluid Mech., **40**(1), pp. 343–366.

[34] Rogallo, R., and Moin, P., 1984, "Numerical Simulation of Turbulent Flows," Annu. Rev. Fluid Mech., **16**(1), pp. 99–137.

[35] Moin, P., and Mahesh, K., 1998, "Direct Numerical Simulation: A Tool in Turbulence Research," Annu. Rev. Fluid Mech., **30**(1), pp. 539–578.

[36] Thomas, S., Esmaeeli, A., and Tryggvason, G., 2010, "Multiscale Computations of Thin Films in Multiphase Flows," Int. J. Multiphase Flow, **36**(1), pp. 71–77.

[37] Perumanath, S., Borg, M., Chubynsky, M., Sprittles, J., and Reese, J., 2019, "Droplet Coalescence is Initiated by Thermal Motion," Phys. Rev. Lett., **122**(10), p. 104501.

[38] Soldati, A., and Marchioli, C., 2009, "Physics and Modelling of Turbulent Particle Deposition and Entrainment: Review of a Systematic Study," Int. J. Multiphase Flow, **35**(9), pp. 827–839.

[39] Roccon, A., De Paoli, M., Zonta, F., and Soldati, A., 2017, "Viscosity-Modulated Breakup and Coalescence of Large Drops in Bounded Turbulence," Phys. Rev. Fluids, **2**(8), p. 083603.

[40] Evrard, F., Denner, F., and van Wachem, B., 2019, "A Hybrid Eulerian-Lagrangian Approach for Simulating Liquid Sprays," ILASS–Europe, Paris, France, 2–4 September 2019.

[41] Xiao, F., Dianat, M., and McGuirk, J., 2014, "LES of Turbulent Liquid Jet Primary Breakup in Turbulent Coaxial Air Flow," Int. J. Multiphase Flow, **60**, pp. 103–118.

[42] Rekvig, L., and Frenkel, D., 2007, "Molecular Simulations of Droplet Coalescence in Oil/Water/Surfactant Systems," J. Chem. Phys., **127**(13), p. 134701.

[43] Svanberg, M., Ming, L., Marković, N., and Pettersson, J. B.-C., 1998, "Collision Dynamics of Large Water Clusters," J. Chem. Phys., **108**(14), pp. 5888–5897.

[44] Balachandar, S., and Eaton, J. K., 2010, "Turbulent Dispersed Multiphase Flow," Annu. Rev. Fluid Mech., **42**(1), pp. 111–133.

[45] Voth, G. A., and Soldati, A., 2017, "Anisotropic Particles in Turbulence," Annu. Rev. Fluid Mech., **49**(1), pp. 249–276.

[46] Herrmann, M., 2010, "Detailed Numerical Simulations of the Primary Atomization of a Turbulent Liquid Jet in Crossflow," ASME J. Eng. Gas Turbine Power, **132**, p. 061506.

[47] Ling, Y., Zaleski, S., and Scardovelli, R., 2015, "Multiscale Simulation of Atomization With Small Droplets Represented by a Lagrangian Point-Particle Model," Int. J. Multiphase Flow, **76**, pp. 122–143.

[48] Herrmann, M., 2013, "A Sub-Grid Surface Dynamics Model for Sub-Filter Surface Tension Induced Interface Dynamics," Comput. Fluids, **87**, pp. 92–101.

[49] Jofre, L., Dodd, M. S., Grau, J., and Torres, R., 2020, "Near-Interface Flow Modeling in Large-Eddy Simulation of Two-Phase Turbulence," Int. J. Multiphase Flow, **132**, p. 103406.

[50] Tryggvason, G., Dabiri, S., Aboulhasanzadeh, B., and Lu, J., 2013, "Multiscale Considerations in Direct Numerical Simulations of Multiphase Flows," Phys. Fluids, 25(3), p. 031302.

[51] Hirt, C., Cook, J., and Butler, T., 1970, "A Lagrangian Method for Calculating the Dynamics of an Incompressible Fluid With Free Surface," J. Comput. Phys., 5(1), pp. 103–124.

[52] Ryskin, G., and Leal, L., 1984, "Numerical Solution of Free-Boundary Problems in Fluid Mechanics. Part 1: The Finite-Difference Technique," J. Fluid Mech., 148, pp. 1–17.

[53] Ryskin, G., and Leal, L., 1984, "Numerical Solution of Free-Boundary Problems in Fluid Mechanics. Part 2: Buoyancy-Driven Motion of a Gas Bubble Through a Quiescent Liquid," J. Fluid Mech., 148, pp. 19–35.

[54] Zonta, F., Soldati, A., and Onorato, M., 2015, "Growth and Spectra of Gravity-Capillary Waves in Countercurrent Air/Water Turbulent Flow," J. Fluid Mech., 777, pp. 245–259.

[55] Glimm, J., 1982, "Tracking of Interfaces for Fluid Flow: Accurate Methods for Piecewise Smooth Problems," Transonic, Shock, and Multidimensional Flows, Academic Press, Cambridge, MA, pp. 259–287.

[56] Glimm, J., and Mcbryan, O. A., 1985, "A Computational Model for Interfaces," Adv. Appl. Math., 6(4), pp. 422–435.

[57] Udaykumar, H. S., Kan, H. C., Shyy, W., and Tran-Son-Tay, R., 1997, "Multiphase Dynamics in Arbitrary Geometries on Fixed Cartesian Grids," J. Comput. Phys., 137(2), pp. 366–405.

[58] Fedkiw, R., Aslam, T., Merriman, B., and Osher, S., 1999, "A Non-Oscillatory Eulerian Approach to Interfaces in Multimaterial Flows (the Ghost Fluid Method)," J. Comput. Phys., 152(2), pp. 457–492.

[59] Lee, L., and LeVeque, R. J., 2003, "An Immersed Interface Method for Incompressible Navier–Stokes Equations," SIAM J. Sci. Comput., 25(3), pp. 832–856.

[60] Leal, G., 2007, Advanced Transport Phenomena: Fluid Mechanics and Convective Transport Processes, Cambridge University Press, Cambridge, UK.

[61] Popinet, S., 2018, "Numerical Models of Surface Tension," Annu. Rev. Fluid Mech., 50(1), pp. 49–75.

[62] Osher, S., and Fedkiw, R., 2003, Level Set Methods and Dynamic Implicit Surfaces, Springer Verlag, Berlin.

[63] Steinthorsson, E., and Tryggvason, G., 1999, "A Front Tracking Scheme for High Density-Ratio Multi-Fluid Flows," 14th Computational Fluid Dynamics Conference, Norfolk, VA, Nov. 1–5, p. 3326.

[64] Tryggvason, G., Scardovelli, R., and Zaleski, S., 2011, Direct Numerical Simulations of Gas-Liquid Multiphase Flows, Cambridge University Press, Cambridge, UK.

[65] Dong, S., and Shen, J., 2012, "A Time-Stepping Scheme Involving Constant Coefficient Matrices for Phase-Field Simulations of Two-Phase Incompressible Flows With Large Density Ratios," J. Comput. Phys., 231(17), pp. 5788–5804.

[66] Fuster, D., 2013, "An Energy Preserving Formulation for the Simulation of Multiphase Turbulent Flows," J. Comput. Phys., 235, pp. 114–128.

[67] Dodd, M. S., and Ferrante, A., 2014, "A Fast Pressure-Correction Method for Incompressible Two-Fluid Flows," J. Comput. Phys., 273, pp. 416–434.

[68] Wang, Z., Dong, S., Triantafyllou, M., Constantinides, Y., and Karniadakis, G., 2019, "A Stabilized Phase-Field Method for Two-Phase Flow at High Reynolds Number and Large Density/Viscosity Ratio," J. Comput. Phys., 397, p. 108832.

[69] Brackbill, J., Kothe, D., and Zemach, C., 1992, "A Continuum Method for Modeling Surface Tension," J. Comput. Phys., 100(2), pp. 335–354.

[70] Sussman, M., Smereka, P., and Osher, S., 1994, "A Level Set Approach for Computing Solutions to Incompressible Two-Phase Flows," J. Comput. Phys., 114(1), pp. 146–159.

[71] Kim, J., 2005, "A Continuous Surface Tension Force Formulation for Diffuse-Interface Models," J. Comput. Phys., 204(2), pp. 784–804.

[72] Kang, I., and Leal, L., 1987, "Numerical Solution of Axisymmetric, Unsteady Free-Boundary Problems at Finite Reynolds Number. I. Finite-Difference Scheme and Its Application to the Deformation of a Bubble in a Uniaxial Straining Flow," Phys. Fluids, 30(7), pp. 1929–1940.

[73] Crowe, C. T., Schwarzkopf, J. D., Sommerfeld, M., and Tsuji, Y., 2011, Multiphase Flows With Droplets and Particles, CRC Press, Boca Raton, FL.

[74] Sussman, M., Smith, K. M., Hussaini, M. Y., Ohta, M., and Zhi-Wei, R., 2007, "A Sharp Interface Method for Incompressible Two-Phase Flows," J. Comput. Phys., 221(2), pp. 469–505.

[75] Popinet, S., and Zaleski, S., 1999, "A Front-Tracking Algorithm for Accurate Representation of Surface Tension," Int. J. Numer. Meth. Flow, 30(6), pp. 775–793.

[76] Hong, J. M., Shinar, T., Kang, M., and Fedkiw, R., 2007, "On Boundary Condition Capturing for Multiphase Interfaces," J. Sci. Comput., 31(1–2), pp. 99–125.

[77] Desjardins, O., Moureau, V., and Pitsch, H., 2008, "An Accurate Conservative Level Set/Ghost Fluid Method for Simulating Turbulent Atomization," J. Comput. Phys., 227(18), pp. 8395–8416.

[78] Tanguy, S., Ménard, T., and Berlemont, A., 2007, "A Level Set Method for Vaporizing Two-Phase Flows," J. Comput. Phys., 221(2), pp. 837–853.

[79] Tanguy, S., Sagan, M., Lalanne, B., Couderc, F., and Colin, C., 2014, "Benchmarks and Numerical Methods for the Simulation of Boiling Flows," J. Comput. Phys., 264, pp. 1–22.

[80] Villegas, L. R., Alis, R., Lepilliez, M., and Tanguy, S., 2016, "A Ghost Fluid/Level Set Method for Boiling Flows and Liquid Evaporation: Application to the Leidenfrost Effect," J. Comput. Phys., 316, pp. 789–813.

[81] Gibou, F., Chen, L., Nguyen, D., and Banerjee, S., 2007, "A Level Set Based Sharp Interface Method for the Multiphase Incompressible Navier–Stokes Equations With Phase Change," J. Comput. Phys., 222(2), pp. 536–555.

[82] Liu, T., Khoo, B., and Yeo, K., 2001, "The Simulation of Compressible Multi-Medium Flow. I. A New Methodology With Test Applications to 1D Gas-Gas and Gas-Water Cases," Comput. Fluids, 30(3), pp. 291–314.

[83] Liu, T., Khoo, B., and Yeo, K., 2001, "The Simulation of Compressible Multi-Medium Flow: II. Applications to 2D Underwater Shock Refraction," Comput. Fluids, 30(3), pp. 315–337.

[84] Liu, T. G., Khoo, B. C., and Yeo, K. S., 2003, "Ghost Fluid Method for Strong Shock Impacting on Material Interface," J. Comput. Phys., 190(2), pp. 651–681.

[85] Ménard, T., Tanguy, S., and Berlemont, A., 2007, "Coupling Level Set/VOF/Ghost Fluid Methods: Validation and Application to 3D Simulation of the Primary Break-Up of a Liquid Jet," Int. J. Multiphase Flow, 33(5), pp. 510–524.

[86] Ge, Z., Loiseau, J. C., Tammisola, O., and Brandt, L., 2018, "An Efficient Mass-Preserving Interface-Correction Level Set/Ghost Fluid Method for Droplet Suspensions Under Depletion Forces," J. Comput. Phys., 353, pp. 435–459.

[87] Helgadóttir, Á., Guittet, A., and Gibou, F., 2018, "On Solving the Poisson Equation With Discontinuities on Irregular Interfaces: GFM and VIM," Int. J. Differ. Equ., 2018, pp. 1–8.

[88] Unverdi, S. O., and Tryggvason, G., 1992, "A Front-Tracking Method for Viscous, Incompressible, Multi-Fluid Flows," J. Comput. Phys., 100(1), pp. 25–37.

[89] Tryggvason, G., Bunner, B., Esmaeeli, A., Juric, D., Al-Rawahi, N., Tauber, W., Han, J., Nas, S., and Jan Y.-J., 2001, "A Front-Tracking Method for the Computations of Multiphase Flow," J. Comput. Phys., 169(2), pp. 708–759.

[90] Nobari, M., and Tryggvason, G., 1996, "Numerical Simulations of Three-Dimensional Drop Collisions," AIAA J., 34(4), pp. 750–755.

[91] Lu, J., and Tryggvason, G., 2018, "Direct Numerical Simulations of Multifluid Flows in a Vertical Channel Undergoing Topology Changes," Phys. Rev. Fluids, 3(8), p. 084401.

[92] Lu, J., and Tryggvason, G., 2019, "Multifluid Flows in a Vertical Channel Undergoing Topology Changes: Effect of Void Fraction," Phys. Rev. Fluids, 4(8), p. 084301.

[93] Nobari, M., Jan, Y.-J., and Tryggvason, G., 1996, "Head-On Collision of Drops—A Numerical Investigation," Phys. Fluids., 8(1), pp. 29–42.

[94] Glimm, J., Grove, J., Li, X. L., and Tan, D., 2000, "Robust Computational Algorithms for Dynamic Interface Tracking in Three Dimensions," SIAM J. Sci. Comput., 21(6), pp. 2240–2256.

[95] Shin, S., and Juric, D., 2002, "Modeling Three-Dimensional Multiphase Flow Using a Level Contour Reconstruction Method for Front Tracking Without Connectivity," J. Comput. Phys., 180(2), pp. 427–470.

[96] Bo, W., Liu, X., Glimm, J., and Li, X., 2011, "A Robust Front Tracking Method: Verification and Application to Simulation of the Primary Breakup of a Liquid Jet," SIAM J. Sci. Comput., 33(4), pp. 1505–1524.

[97] Peskin, C., 1973, "Flow Patterns Around Heart Valves: A Digital Computer Method for Solving the Equations of Motion," Ph.D. thesis, Yeshiva University, New York.

[98] Iaccarino, G., and Verzicco, R., 2003, "Immersed Boundary Technique for Turbulent Flow Simulations," ASME Appl. Mech. Rev., 56(3), pp. 231–347.

[99] Mittal, R., and Iaccarino, G., 2005, "Immersed Boundary Methods," Annu. Rev. Fluid Mech., 37(1), pp. 239–261.

[100] Sardina, G., Schlatter, P., Brandt, L., Picano, F., and Casciola, C. M., 2012, "Wall Accumulation and Spatial Localization in Particle-Laden Wall Flows," J. Fluid Mech., 699(1), pp. 50–78.

[101] Costa, P., Boersma, B. J., Westerweel, J., and Breugem, W.-P., 2015, "Collision Model for Fully Resolved Simulations of Flows Laden With Finite-Size Particles," Phys. Rev. E, 92(5), p. 053012.

[102] Picano, F., Breugem, W.-P., and Brandt, L., 2015, "Turbulent Channel Flow of Dense Suspensions of Neutrally Buoyant Spheres," J. Fluid Mech., 764, pp. 463–487.

[103] Kim, Y., and Peskin, C. S., 2008, "Numerical Study of Incompressible Fluid Dynamics With Nonuniform Density by the Immersed Boundary Method," Phys. Fluids, 20(6), p. 062101.

[104] Chong, K., Li, Y., Shen, N. C., Verzicco, R., and Lohse, D., 2020, "Convection-Dominated Dissolution for Single and Multiple Immersed Sessile Droplets," J. Fluid Mech., 892, p. A21.

[105] Spandan, V., Meschini, V., Ostilla-Mónico, R., Detlef, L., Querzoli, G., de Tullio, M., and Verzicco, R., 2017, "A Parallel Interaction Potential Approach Coupled With the Immersed Boundary Method for Fully Resolved Simulations of Deformable Interfaces and Membranes," J. Comput. Phys., 348, pp. 567–590.

[106] Spandan, V., Detlef, L., de Tullio, M., and Verzicco, R., 2018, "A Fast Moving Least Squares Approximation With Adaptive Lagrangian Mesh Refinement for Large Scale Immersed Boundary Simulations," J. Comput. Phys., 375, pp. 228–239.

[107] Musong, S., Feng, Z.-G., Michaelides, E., and Mao, S., 2016, "Application of a Three-Dimensional Immersed Boundary Method for Free Convection From Single Spheres and Aggregates," J. Fluid Eng., 138, pp. 1–10.

[108] Peng, S., Spandan, V., Verzicco, R., Detlef, L., and Zhang, X., 2018, "Growth Dynamics of Microbubbles on Microcavity Arrays by Solvent Exchange: Experiments and Numerical Simulations," J. Colloid. Interface Sci., 532, pp. 103–111.

[109] Hirt, C., Amsden, A., and Cook, J., 1974, "An Arbitrary Lagrangian-Eulerian Computing Method for All Flow Speeds," J. Comput. Phys., 14(3), pp. 227–253.

[110] Hu, H., Patankar, N., and Zhu, M., 2001, "Direct Numerical Simulations of Fluid-Solid Systems Using the Arbitrary Lagrangian-Eulerian Technique," J. Comput. Phys., 169(2), pp. 427–462.

[111] Yue, P., Feng, J., Bertelo, C., and Hu, H., 2007, "An Arbitrary Lagrangian-Eulerian Method for Simulating Bubble Growth in Polymer Foaming," J. Comput. Phys., **226**(2), pp. 2229–2249.

[112] Boscheri, W., and Dumbser, M., 2014, "A Direct Arbitrary-Lagrangian-Eulerian ADER-WENO Finite Volume Scheme on Unstructured Tetrahedral Meshes for Conservative and Non-Conservative Hyperbolic Systems in 3D," J. Comput. Phys., **275**, pp. 484–523.

[113] Anjos, G., Mangiavacchi, N., and Thome, J., 2020, "An ALE-FE Method for Two-Phase Flows With Dynamic Boundaries," Comput. Methods Appl. Mech. Eng., **362**, p. 112820.

[114] Cheng, Z., Li, J., Loh, C., and Luo, L.-S., 2020, "An Exactly Force-Balanced Boundary-Conforming Arbitrary-Lagrangian-Eulerian Method for Interfacial Dynamics," J. Comput. Phys., **408**, p. 109237.

[115] Yang, X., and James, A., 2007, "An Arbitrary Lagrangian-Eulerian (ALE) Method for Interfacial Flows With Insoluble Surfactants," FDMP, **3**, pp. 65–96.

[116] Hirt, C., and Nichols, B., 1981, "Volume of Fluid (VOF) Method for the Dynamics of Free Boundaries," J. Comput. Phys., **39**(1), pp. 201–225.

[117] Rider, W., and Kothe, D., 1998, "Reconstructing Volume Tracking," J. Comput. Phys., **141**(2), pp. 112–152.

[118] Xiao, F., Honma, Y., and Kono, T., 2005, "A Simple Algebraic Interface Capturing Scheme Using Hyperbolic Tangent Function," Int. J. Numer. Methods Fluids, **48**(9), pp. 1023–1040.

[119] Ashgriz, N., and Poo, J., 1991, "FLAIR: Flux Line-Segment Model for Advection and Interface Reconstruction," J. Comput. Phys., **93**(2), pp. 449–468.

[120] Noh, W., and Woodward, P., 1976, "SLIC (Simple Line Interface Calculation)," Proceedings of Fifth International Conference on Numerical Methods in Fluid Dynamics, Vol. 59, Twente University, Enschede, The Netherlands, June 28–July 2, pp. 330–340.

[121] Fuster, D., Agbaglah, G., Josserand, C., Popinet, S., and Zaleski, S., 2009, "Numerical Simulation of Droplets, Bubbles and Waves: State of the Art," Fluid Dyn. Res., **41**(6), p. 065001.

[122] Osher, S., and Sethian, J., 1988, "Fronts Propagating With Curvature-Dependent Speed: Algorithms Based on Hamilton-Jacobi Formulations," J. Comput. Phys., **79**(1), pp. 12–49.

[123] Osher, S., and Sethian, J., 1994, "A Level Set Approach for Computing Solutions to Incompressible Two-Phase Flow," J. Comput. Phys., **114**, pp. 12–49.

[124] Osher, S., and Fedkiw, R., 2001, "Level Set Methods: An Overview and Some Recent Results," J. Comput. Phys., **169**(2), pp. 463–502.

[125] Gibou, F., Fedkiw, R., and Osher, S., 2018, "A Review of Level-Set Methods and Some Recent Applications," J. Comput. Phys., **353**, pp. 82–109.

[126] Shu, C., and Osher, S., 1989, "Efficient Implementation of Essentially Non-Oscillatory Shock Capturing Schemes, II," J. Comput. Phys., **83**(1), pp. 32–78.

[127] Sussman, M., and Hussaini, M. Y., 2003, "A Discontinuous Spectral Element Method for the Level Set Equation," J. Sci. Comput., **19**(1/3), pp. 479–500.

[128] Chang, Y., Hou, T., Merriman, B., and Osher, S., 1996, "Eulerian Capturing Methods Based on a Level Set Formulation for Incompressible Fluid Interfaces," J. Comput. Phys., **124**(2), pp. 449–464.

[129] Sethian, J., 1999, Level Set Methods and Fast Marching Methods: Evolving Interfaces in Computational Geometry, Fluid Mechanics, Computer Vision, and Materials Science, Vol. 3, Cambridge University Press, Cambridge, UK.

[130] Sussman, M., and Fatemi, E., 1999, "An Efficient, Interface Preserving Level Set Redistancing Algorithm and Its Application to Interfacial Incompressible Fluid Flow," SIAM J. Sci. Comput., **20**(4), pp. 1165–1191.

[131] Herrmann, M., 2008, "A Balanced Force Refined Level Set Grid Method for Two-Phase Flows on Unstructured Flow Solver Grids," J. Comput. Phys., **227**(4), pp. 2674–2706.

[132] Olsson, E., and Kreiss, G., 2005, "A Conservative Level Set Method for Two Phase Flow," J. Comput. Phys., **210**(1), pp. 225–246.

[133] Sussman, M., and Puckett, E. G., 2000, "A Coupled Level Set and Volume-of-Fluid Method for Computing 3D and Axisymmetric Incompressible Two-Phase Flows," J. Comput. Phys., **162**(2), pp. 301–337.

[134] Sussman, M., 2003, "A Second Order Coupled Level-Set and Volume of Fluid Method for Computing Growth and Collapse of Vapor Bubbles," J. Comput. Phys., **187**(1), pp. 110–136.

[135] Cahn, J., and Hilliard, J., 1958, "Free Energy of a Nonuniform System—I: Interfacial Free Energy," J. Chem. Phys., **28**(2), pp. 258–267.

[136] Cahn, J., and Hilliard, J., 1959, "Free Energy of a Nonuniform System—II: Thermodynamic Basis," J. Chem. Phys., **30**(5), pp. 1121–1124.

[137] Cahn, J., and Hilliard, J., 1959, "Free Energy of a Nonuniform System—III: Nucleation in a Two-Component Incompressible Fluid," J. Chem. Phys., **31**(3), pp. 688–699.

[138] Jacqmin, D., 1999, "Calculation of Two-Phase Navier–Stokes Flows Using Phase-Field Modeling," J. Comput. Phys., **155**(1), pp. 96–127.

[139] Jacqmin, D., 2000, "Contact-Line Dynamics of a Diffuse Fluid Interface," J. Fluid Mech., **402**, pp. 57–88.

[140] Badalassi, V., Ceniceros, H., and Banerjee, S., 2003, "Computation of Multiphase Systems With Phase Field Models," J. Comput. Phys., **190**(2), pp. 371–397.

[141] Kim, J., and Lowengrub, J., 2005, "Phase Field Modeling and Simulation of Three-Phase Flows," Interfaces Free Bound., **7**(4), p. 435.

[142] Ding, H., Spelt, P., and Shu, C., 2007, "Diffuse Interface Model for Incompressible Two-Phase Flows With Large Density Ratios," J. Comput. Phys., **226**(2), pp. 2078–2095.

[143] Shen, J., and Yang, X., 2010, "A Phase-Field Model and Its Numerical Approximation for Two-Phase Incompressible Flows With Different Densities and Viscosities," SIAM J. Sci. Comput., **32**(3), pp. 1159–1179.

[144] Chen, L., 2002, "Phase-Field Models for Microstructure Evolution," Annu. Rev. Mater. Res., **32**(1), pp. 113–140.

[145] Magaletti, F., Picano, F., Chinappi, M., Marino, L., and Casciola, C., 2013, "The Sharp-Interface Limit of the Cahn–Hilliard/Navier–Stokes Model for Binary Fluids," J. Fluid Mech., **714**, pp. 95–126.

[146] Yue, P., Zhou, C., and Feng, J., 2007, "Spontaneous Shrinkage of Drops and Mass Conservation in Phase-Field Simulations," J. Comput. Phys., **223**(1), pp. 1–9.

[147] Li, Y., Choi, J., and Kim, J., 2016, "A Phase-Field Fluid Modeling and Computation With Interfacial Profile Correction Term," Commun. Nonlinear Sci., **30**(1–3), pp. 84–100.

[148] Zhang, Y., and Ye, W., 2017, "A Flux-Corrected Phase-Field Method for Surface Diffusion," Commun. Comput. Phys., **22**(2), pp. 422–440.

[149] Soligo, G., Roccon, A., and Soldati, A., 2019, "Mass-Conservation-Improved Phase Field Methods for Turbulent Multiphase Flow Simulation," Acta Mech., **230**(2), pp. 683–696.

[150] Lamorgese, A., Mauri, R., and Sagis, L., 2017, "Modeling Soft Interface Dominated Systems: A Comparison of Phase Field and Gibbs Dividing Surface Models," Phys. Rep., **675**, pp. 1–54.

[151] Mirjalili, S., Ivey, C., and Mani, A., 2019, "Comparison Between the Diffuse Interface and Volume of Fluid Methods for Simulating Two-Phase Flows," Int. J. Multiphase Flow, **116**, pp. 221–238.

[152] Soligo, G., Roccon, A., and Soldati, A., 2019, "Breakage, Coalescence and Size Distribution of Surfactant-Laden Droplets in Turbulent Flow," J. Fluid Mech., **881**, pp. 244–282.

[153] Mukherjee, S., Safdari, A., Shardt, O., Kenjereš, S., and Van den Akker, H., 2019, "Droplet–Turbulence Interactions and Quasi-Equilibrium Dynamics in Turbulent Emulsions," J. Fluid Mech., **878**, pp. 221–276.

[154] Huang, K., 1963, Statistical Mechanics, Wiley, Hoboken, NJ.

[155] Cercignani, C., 1969, Mathematical Methods in Kinetic Theory, Plenum Press, New York.

[156] Liboff, R., 1969, Introduction to the Theory of Kinetic Equations, Wiley, Hoboken, NJ.

[157] Chapman, S., and Cowling, T., 1970, The Mathematical Theory of Non-Uniform Gases, Cambridge University Press, Cambridge, UK.

[158] Koga, T., 1970, Introduction to Kinetic Theory Stochastic Processes in Gaseous Systems, Pergamon Press, Oxford, UK.

[159] Harris, S., 1971, An Introduction to the Theory of the Boltzmann Equation, Rinehart and Winston, New York.

[160] He, X., and Luo, L.-S., 1997, "Theory of the Lattice Boltzmann Method: From the Boltzmann Equation to the Lattice Boltzmann Equation," Phys. Rev. E, **56**(6), pp. 6811–6817.

[161] Nourgaliev, R. R., Dinh, T. N., Theofanous, T. G., and Joseph, D., 2003, "The Lattice Boltzmann Equation Method: Theoretical Interpretation, Numerics and Implications," Int. J. Multiphase Flow, **29**(1), pp. 117–169.

[162] Chen, S., and Doolen, G., 1998, "Lattice Boltzmann Method for Fluid Flows," Annu. Rev. Fluid Mech., **30**(1), pp. 329–364.

[163] Aidun, C., and Clausen, J., 2010, "Lattice-Boltzmann Method for Complex Flows," Annu. Rev. Fluid Mech., **42**(1), pp. 439–472.

[164] Zhang, J., 2011, "Lattice Boltzmann Method for Microfluidics: Models and Applications," Microfluid. Nanofluid., **10**(1), pp. 1–28.

[165] Li, Q., Luo, K. H., Kang, Q., He, Y., Chen, Q., and Liu, Q., 2016, "Lattice Boltzmann Methods for Multiphase Flow and Phase-Change Heat Transfer," Prog. Energy Combust. Sci., **52**, pp. 62–105.

[166] Rothman, D., and Keller, J., 1988, "Immiscible Cellular-Automaton Fluids," J. Stat. Phys., **52**(3–4), pp. 1119–1127.

[167] Gunstensen, A. K., Rothman, D. H., Zaleski, S., and Zanetti, G., 1991, "Lattice Boltzmann Model of Immiscible Fluids," Phys. Rev. A, **43**(8), pp. 4320–4327.

[168] Grunau, D., Chen, S., and Eggert, K., 1993, "A Lattice Boltzmann Model for Multiphase Fluid Flows," Phys. Fluids A, **5**(10), pp. 2557–2562.

[169] Shan, X., and Chen, H., 1993, "Lattice Boltzmann Model for Simulating Flows With Multiple Phases and Components," Phys. Rev. E, **47**(3), pp. 1815–1819.

[170] Shan, X., and Chen, H., 1994, "Simulation of Nonideal Gases and Liquid-Gas Phase Transitions by the Lattice Boltzmann Equation," Phys. Rev. E, **49**(4), pp. 2941–2948.

[171] Shan, X., and Doolen, G., 1995, "Multicomponent Lattice-Boltzmann Model With Interparticle Interaction," J. Stat. Phys., **81**(1–2), pp. 379–393.

[172] Orlandini, S., Swift, M., and Yeomans, J., 1995, "A Lattice Boltzmann Model for Binary-Fluid Mixtures," Europhys. Lett., **32**(6), pp. 463–468.

[173] Swift, M., Orlandini, S., Osborn, W., and Yeomans, J., 1996, "Lattice Boltzmann Simulations of Liquid-Gas and Binary Fluid Systems," Phys. Rev. E, **54**(5), pp. 5041–5052.

[174] He, X., Chen, S., and Doolen, G., 1998, "A Novel Thermal Model for the Lattice Boltzmann Method in Incompressible Limit," J. Comput. Phys., **146**(1), pp. 282–300.

[175] He, X., Chen, S., and Zhang, R., 1999, "A Lattice Boltzmann Scheme for Incompressible Multiphase Flow and Its Application in Simulation of Rayleigh-Taylor Instability," J. Comput. Phys., **152**(2), pp. 642–663.

[176] He, X., Zhang, R., Chen, S., and Doolen, G., 1999, "On the Three-Dimensional Rayleigh–Taylor Instability," Phys. Fluids, **11**(5), pp. 1143–1152.

[177] Zhang, R., He, X., Doolen, G., and Chen, S., 2001, "Surface Tension Effects on Two-Dimensional Two-Phase Kelvin-Helmholtz Instabilities," Adv. Water Resource, **24**(3–4), pp. 461–478.

[178] Chin, J., Boek, E., and Coveney, P., 2002, "Lattice Boltzmann Simulation of the Flow of Binary Immiscible Fluids With Different Viscosities Using the

Shan-Chen Microscopic Interaction Model," Philos. Trans. R. Soc. A, **360**(1792), pp. 547–558.

[179] Kang, Q., Zhang, D., and Chen, S., 2002, "Displacement of a Two-Dimensional Immiscible Droplet in a Channel," Phys. Fluids, **14**, pp. 203–214.

[180] Kang, Q., Zhang, D., and Chen, S., 2004, "Immiscible Displacement in a Channel: Simulations of Fingering in Two Dimensions," Adv. Water. Resource, **27**(1), pp. 13–22.

[181] Inamuro, T., Ogata, T., Tajima, S., and Konishi, N., 2004, "A Lattice Boltzmann Method for Incompressible Two-Phase Flows With Large Density Differences," J. Comput. Phys., **198**(2), pp. 628–644.

[182] Zheng, H., Shu, C., and Chew, Y., 2006, "A Lattice Boltzmann Model for Multiphase Flows With Large Density Ratio," J. Comput. Phys., **218**(1), pp. 353–371.

[183] Lee, T., and Lin, C., 2005, "A Stable Discretization of the Lattice Boltzmann Equation for Simulation of Incompressible Two-Phase Flows at High Density Ratio," J. Comput. Phys., **206**(1), pp. 16–47.

[184] Levich, V. G., and Seeger, R. J., 1963, "Physicochemical Hydrodynamics," Am. J. Phys., **31**(11), pp. 892–892.

[185] Manikantan, H., and Squires, T. M., 2020, "Surfactant Dynamics: Hidden Variables Controlling Fluid Flows," J. Fluid Mech., **892**(P1), pp. 1–115.

[186] Stone, H., 1990, "A Simple Derivation of the Time Dependent Convective Diffusion Equation for Surfactant Transport Along a Deforming Interface," Phys. Fluids A, **2**(1), pp. 111–112.

[187] Slattery, J., Sagis, L., and Oh, E., 2007, *Interfacial Transport Phenomena*, Springer Science & Business Media, Berlin (DE).

[188] Lai, M., Tseng, Y., and Huang, H., 2008, "An Immersed Boundary Method for Interfacial Flows With Insoluble Surfactant," J. Comput. Phys., **227**(15), pp. 7279–7293.

[189] Lai, M., Tseng, Y., and Huang, H., 2010, "Numerical Simulation of Moving Contact Lines With Surfactant by Immersed Boundary Method," Commun. Comput. Phys., **8**(4), pp. 735–757.

[190] Lu, J., Muradoglu, M., and Tryggvason, G., 2017, "Effect of Insoluble Surfactant on Turbulent Bubbly Flows in Vertical Channels," Int. J. Multiphase Flow, **95**, pp. 135–143.

[191] Piedfert, A., Lalanne, B., Masbernat, O., and Risso, F., 2018, "Numerical Simulations of a Rising Drop With Shape Oscillations in the Presence of Surfactants," Phys. Rev. Fluids, **3**(10), p. 103605.

[192] Renardy, Y., Renardy, M., and Cristini, V., 2002, "A New Volume-of-Fluid Formulation for Surfactants and Simulations of Drop Deformation Under Shear at a Low Viscosity Ratio," Eur. J. Mech. B-Fluid, **21**(1), pp. 49–59.

[193] Xu, J.-J., and Zhao, H., 2003, "An Eulerian Formulation for Solving Partial Differential Equations Along a Moving Interface," SIAM J. Sci. Comput., **19**(1/3), pp. 573–594.

[194] James, A., and Lowengrub, J., 2004, "A Surfactant-Conserving Volume-of-Fluid Method for Interfacial Flows With Insoluble Surfactant," J. Comput. Phys., **201**(2), pp. 685–722.

[195] Ganesan, S., and Tobiska, L., 2009, "A Coupled Arbitrary Lagrangian–Eulerian and Lagrangian Method for Computation of Free Surface Flows With Insoluble Surfactants," J. Comput. Phys., **228**(8), pp. 2859–2873.

[196] Farhat, H., Celiker, F., Singh, T., and Lee, J., 2011, "A Hybrid Lattice Boltzmann Model for Surfactant-Covered Droplets," Soft Matter, **7**(5), pp. 1968–1985.

[197] Xu, J.-J., Li, Z., Lowengrub, J., and Zhao, H., 2011, "Numerical Study of Surfactant-Laden Drop-Drop Interactions," Commun. Comput. Phys., **10**(2), pp. 453–473.

[198] Xu, J.-J., Yang, Y., and Lowengrub, J., 2012, "A Level-Set Continuum Method for Two-Phase Flows With Insoluble Surfactant," J. Comput. Phys., **231**(17), pp. 5897–5909.

[199] Xu, J.-J., and Ren, W., 2014, "A Level-Set Method for Two-Phase Flows With Moving Contact Line and Insoluble Surfactant," J. Comput. Phys., **263**, pp. 71–90.

[200] Liu, H., Ba, Y., Wu, L., Li, Z., Xi, G., and Zhang, Y., 2018, "A Hybrid Lattice Boltzmann and Finite Difference Method for Droplet Dynamics With Insoluble Surfactants," J. Fluid Mech., **837**, pp. 381–412.

[201] Zhang, J., Eckmann, D., and Ayyaswamy, P., 2006, "A Front Tracking Method for a Deformable Intravascular Bubble in a Tube With Soluble Surfactant Transport," J. Comput. Phys., **214**(1), pp. 366–396.

[202] Muradoglu, M., and Tryggvason, G., 2014, "Simulations of Soluble Surfactants in 3D Multiphase Flow," J. Comput. Phys., **274**, pp. 737–757.

[203] Ahmed, Z., Izbassarov, D., Costa, P., Muradoglu, M., and Tammisola, O., 2020, "Turbulent Bubbly Channel Flows: Effects of Soluble Surfactant and Viscoelasticity," Comp. Fluids, **212**, p. 104717.

[204] Teigen, K., Li, X., Lowengrub, J., Wang, F., and Voigt, A., 2009, "A Diffuse-Interface Approach for Modeling Transport, Diffusion and Adsorption/Desorption of Material Quantities on a Deformable Interface," Commun. Math. Sci., **7**(4), pp. 1009–1037.

[205] Ganesan, S., and Tobiska, L., 2012, "Arbitrary Lagrangian–Eulerian Finite-Element Method for Computation of Two-Phase Flows With Soluble Surfactants," J. Comput. Phys., **231**(9), pp. 3685–3702.

[206] Porter, M. R., 1991, *Handbook of Surfactants*, Springer, New York.

[207] Chang, C., and Franses, E., 1995, "Adsorption Dynamics of Surfactants at the Air/Water Interface: A Critical Review of Mathematical Models, Data, and Mechanisms," Colloids Surf. A, **100**, pp. 1–45.

[208] López-Díaz, D., García-Mateos, I., and Velázquez, M. M., 2006, "Surface Properties of Mixed Monolayers of Sulfobetaines and Ionic Surfactants," J. Colloid Interface Sci., **299**(2), pp. 858–866.

[209] Ju, H., Jiang, Y., Geng, T., Wang, Y., and Zhang, C., 2017, "Equilibrium and Dynamic Surface Tension of Quaternary Ammonium Salts With Different Hydrocarbon Chain Length of Counterions," J. Mol. Liq., **225**, pp. 606–612.

[210] Komura, S., and Kodama, H., 1997, "Two-Order-Parameter Model for an Oil-Water-Surfactant System," Phys. Rev. E, **55**(2), pp. 1722–1727.

[211] Engblom, S., Do-Quang, M., Amberg, G., and Tornberg, A., 2013, "On Diffuse Interface Modeling and Simulation of Surfactants in Two-Phase Fluid Flow," Commun. Comput. Phys., **14**(4), pp. 879–915.

[212] Yun, A., Li, Y., and Kim, J., 2014, "A New Phase-Field Model for a Water-Oil-Surfactant System," Appl. Math. Comput., **229**, pp. 422–432.

[213] Laradji, M., Guo, H., Grant, M., and Zuckermann, M., 1992, "The Effect of Surfactants on the Dynamics of Phase Separation," J. Phys. Conden. Matter, **4**(32), pp. 6715–6728.

[214] Liu, H., and Zhang, Y., 2010, "Phase-Field Modeling Droplet Dynamics With Soluble Surfactants," J. Comput. Phys., **229**(24), pp. 9166–9187.

[215] Soligo, G., Roccon, A., and Soldati, A., 2020, "Effect of Surfactant-Laden Droplets on Turbulent Flow Topology," Phys. Rev. Fluids, **5**(7), p. 073606.

[216] Murad, S., and Law, C., 1999, "Molecular Simulation of Droplet Collision in the Presence of Ambient Gas," Mol. Phys., **96**(1), pp. 81–85.

[217] MacKay, G., and Mason, S., 1963, "The Gravity Approach and Coalescence of Fluid Drops at Liquid Interfaces," Can. J. Chem. Eng., **41**(5), pp. 203–212.

[218] Gotaas, C., Havelka, P., Jakobsen, H., Svendsen, H., Hase, M., Roth, N., and Weigand, B., 2007, "Effect of Viscosity on Droplet-Droplet Collision Outcome: Experimental Study and Numerical Comparison," Phys. Fluids, **19**(10), p. 102106.

[219] Chen, N., Kuhl, T., Tadmor, R., Lin, Q., and Israelachvili, J., 2004, "Large Deformations During the Coalescence of Fluid Interfaces," Phys. Rev. Lett., **92**(2), p. 024501.

[220] Aarts, D., Schmidt, M., and Lekkerkerker, H., 2004, "Direct Visual Observation of Thermal Capillary Waves," Sci., **304**(5672), pp. 847–850.

[221] Aarts, D., Lekkerkerker, H. N., Guo, H., Wegdam, C., and Bonn, D., 2005, "Hydrodynamics of Droplet Coalescence," Phys. Rev. Lett., **95**(16), p. 164503.

[222] Zdravkov, A., Peters, G., and Meijer, H., 2006, "Film Drainage and Interfacial Instabilities in Polymeric Systems With Diffuse Interfaces," J. Colloid Interface Sci., **296**(1), pp. 86–94.

[223] Dodd, M., and Ferrante, A., 2016, "On the Interaction of Taylor Length Scale Size Droplets and Isotropic Turbulence," J. Fluid Mech., **806**, pp. 356–412.

[224] Rosti, M., De Vita, F., and Brandt, L., 2019, "Numerical Simulations of Emulsions in Shear Flows," Acta Mech., **230**(2), pp. 667–682.

[225] Rosti, M., Ge, Z., Jain, S., Dodd, M., and Brandt, L., 2019, "Droplets in Homogeneous Shear Turbulence," J. Fluid Mech., **876**, pp. 962–984.

[226] Ashgriz, N., and Poo, J., 1990, "Coalescence and Separation in Binary Collisions of Liquid Drops," J. Fluid Mech., **221**, pp. 183–204.

[227] Soldati, A., and Andreussi, P., 1996, "The Influence of Coalescence on Droplet Transfer in Vertical Annular Flow," Chem. Eng. Sci., **51**(3), pp. 353–363.

[228] Tryggvason, G., Thomas, S., Lu, J., and Aboulhasanzadeh, B., 2010, "Multiscale Issues in DNS of Multiphase Flows," Acta Math. Sci., **30**(2), pp. 551–562.

[229] Charles, G., and Mason, S., 1960, "The Coalescence of Liquid Drops With Flat Liquid/Liquid Interfaces," J. Colloid Sci., **15**(3), pp. 236–267.

[230] Allan, R., Charles, G., and Mason, S., 1961, "The Approach of Gas Bubbles to a Gas/Liquid Interface," J. Colloid Sci., **16**(2), pp. 150–165.

[231] Kwakkel, M., Breugem, W.-P., and Boersma, B., 2013, "Extension of a CLSVOF Method for Droplet-Laden Flows With a Coalescence/Breakup Model," J. Comput. Phys., **253**, pp. 166–188.

[232] Hahn, P.-S., and Slattery, J. C., 1985, "Effects of Surface Viscosities on the Stability of a Draining Plane Parallel Liquid Film as a Small Bubble Approaches a Liquid-Gas Interface," AIChE J., **31**(6), pp. 950–956.

[233] Liu, M., and Bothe, D., 2019, "Toward the Predictive Simulation of Bouncing Versus Coalescence in Binary Droplet Collisions," Acta Mech., **230**(2), pp. 623–644.

[234] Zhang, P., and Law, C. K., 2011, "An Analysis of Head-on Droplet Collision With Large Deformation in Gaseous Medium," Phys. Fluids, **23**(4), p. 042102.

[235] De Vita, F., Rosti, M., Caserta, S., and Brandt, L., 2019, "On the Effect of Coalescence on the Rheology of Emulsions," J. Fluid Mech., **880**, pp. 969–991.

[236] Montessori, A., Lauricella, M., Tirelli, N., and Succi, S., 2019, "Mesoscale Modelling of Near-Contact Interactions for Complex Flowing Interfaces," J. Fluid Mech., **872**, pp. 327–347.

[237] Talley, M., Zimmer, M., and Bolotnov, I., 2017, "Coalescence Prevention Algorithm for Level-Set Method," ASME J. Fluids Eng., **139**(8), p. 081301.

[238] O'Rourke, P. J., 1981, "Collective Drop Effects on Vaporizing Liquid Sprays," Ph.D. thesis, Princeton University, Princeton, NJ.

[239] Ko, G. H., Ryou, H. S., Hur, N. K., Ko, S. W., and Youn, M. O., 2007, "Numerical Study on Bouncing and Separation Collision Between Two Droplets Considering the Collision-Induced Breakup," J. Mech. Sci. Technol., **21**(4), pp. 585–592.

[240] Brazier-Smith, P. R., Jennings, S. G., and Latham, J., 1972, "The Interaction of Falling Water Drops: Coalescence," Proc. R. Soc. Lond. A, **326**, pp. 393–408.

[241] Notz, P., and Basaran, O., 2004, "Dynamics and Breakup of a Contracting Liquid Filament," J. Fluid Mech., **512**, pp. 223–256.

[242] Anthony, C. R., Kamat, P. M., Harris, M. T., and Basaran, O. A., 2019, "Dynamics of Contracting Filaments," Phys. Rev. Fluids, **4**(9), p. 093601.

[243] Eggers, J., 1995, "Theory of Drop Formation," Phys. Fluids, **7**(5), pp. 941–953.

[244] Eggers, J., 1997, "Nonlinear Dynamics and Breakup of Free-Surface Flows," Rev. Mod. Phys., **69**(3), pp. 865–930.

[245] Herrmann, M., 2011, "On Simulating Primary Atomization Using the Refined Level Set Grid Method," Atom. Spray, **21**(4), pp. 283–301.

[246] Kim, D., Desjardins, O., Herrmann, M., and Moin, P., 2006, "Toward Two-Phase Simulation of the Primary Breakup of a Round Liquid Jet by a Coaxial Flow of Gas," Cent. Turbul. Res. Annu. Res. Briefs, pp. 185–195.

[247] Tomar, G., Fuster, D., Zaleski, S., and Popinet, S., 2010, "Multiscale Simulations of Primary Atomization," Comput. Fluids, **39**(10), pp. 1864–1864.

[248] Apte, S., Gorokhovski, M., and Moin, P., 2003, "LES of Atomizing Spray With Stochastic Modeling of Secondary Breakup," Int. J. Multiphase Flow, **29**(9), pp. 1503–1522.

[249] Herrmann, M., 2003, "Modeling Primary Breakup: A Three-Dimensional Eulerian Level Set/Vortex Sheet Method for Two-Phase Interface Dynamics," Cent. Turbul. Res. Annu. Res. Briefs, pp. 185–196.

[250] Clift, R., Grace, J. R., and Weber, M. E., 2005, *Bubbles, Drops, and Particles*, Courier Corporation, Chelmsford, MA.

[251] Maffettone, P., and Minale, M., 1998, "Equation of Change for Ellipsoidal Drops in Viscous Flow," J. Non-Newton. Fluid Mech., **78**(2–3), pp. 227–241.

[252] Cristini, V., Błaczdziewicz, J., Loewenberg, M., and Collins, L. R., 2003, "Breakup in Stochastic Stokes Flows: Sub-Kolmogorov Drops in Isotropic Turbulence," J. Fluid Mech., **492**, pp. 231–250.

[253] Biferale, L., Meneveau, C., and Verzicco, R., 2014, "Deformation Statistics of Sub-Kolmogorov-Scale Ellipsoidal Neutrally Buoyant Drops in Isotropic Turbulence," J. Fluid Mech., **754**, pp. 184–207.

[254] Spandan, V., Lohse, D., and Verzicco, R., 2016, "Deformation and Orientation Statistics of Neutrally Buoyant Sub-Kolmogorov Ellipsoidal Droplets in Turbulent Taylor–Couette Flow," J. Fluid Mech., **809**, pp. 480–501.

[255] Spandan, V., Verzicco, R., and Lohse, D., 2017, "Deformable Ellipsoidal Bubbles in Taylor–Couette Flow With Enhanced Euler-Lagrangian Tracking," Phys. Rev. Fluids, **2**(10), p. 104304.

[256] Rosen, M., and Kunjappu, J., 2012, *Surfactants and Interfacial Phenomena*, Wiley, Hoboken, NJ.

[257] Hinze, J., 1955, "Fundamentals of the Hydrodynamic Mechanism of Splitting in Dispersion Processes," AIChE J., **1**(3), pp. 289–295.

[258] Masuk, A., Salibindla, A., and Ni, R., 2021, "Simultaneous Measurements of Deforming Hinze-Scale Bubbles With Surrounding Turbulence," J. Fluid Mech., **910**, p. A21.

[259] Lycett-Brown, D., Luo, K., Liu, R., and Lv, P., 2014, "Binary Droplet Collision Simulations by a Multiphase Cascaded Lattice Boltzmann Method," Phys. Fluids, **26**(2), p. 023303.

[260] Qian, J., and Law, C. K., 1997, "Regimes of Coalescence and Separation in Droplet Collision," J. Fluid Mech., **331**, pp. 59–80.

[261] Rajkotwala, A. H., Mirsandi, H., Peters, E. A. J. F., Baltussen, M. W., Van der Geld, C. W. M., Kuerten, J. G. M., and Kuipers, J. A. M., 2018, "Extension of Local Front Reconstruction Method With Controlled Coalescence Model," Phys. Fluids, **30**(2), p. 022102.

[262] Jiang, Y. J., Umemura, A., and Law, C. K., 1992, "An Experimental Investigation on the Collision Behaviour of Hydrocarbon Droplets," J. Fluid Mech., **234**(1), pp. 171–190.

[263] Sommerfeld, M., and Kuschel, M., 2016, "Modelling Droplet Collision Outcomes for Different Substances and Viscosities," Exp. Fluids, **57**(12), p. 187.

[264] Finotello, G., Padding, J., Deen, N., Jongsma, A., Innings, F., and Kuipers, J., 2017, "Effect of Viscosity on Droplet-Droplet Collisional Interaction," Phys. Fluids, **29**(6), p. 067102.

[265] Finotello, G., Kooiman, R., Padding, J., Buist, K., Jongsma, A., Innings, F., and Kuipers, J., 2018, "The Dynamics of Milk Droplet–Droplet Collisions," Exp. Fluids, **59**(1), p. 17.

[266] Al-Dirawi, K., and Bayly, A., 2019, "A New Model for the Bouncing Regime Boundary in Binary Droplet Collisions," Phys. Fluids, **31**(2), p. 027105.

[267] Pan, K., Law, C., and Zhou, B., 2008, "Experimental and Mechanistic Description of Merging and Bouncing in Head-on Binary Droplet Collision," J. Appl. Phys., **103**(6), p. 064901.

[268] Sussmann, M., 1994, "A Level Set for Computing Solutions to Incompressible Two-Phase Flow," Ph.D. thesis, University of California, Los Angeles, CA.

[269] Rajkotwala, A. H., Gelissen, E. J., Peters, E. A. J. F., Baltussen, M. W., van der Geld, C. W. M., Kuerten, J. G. M., and Kuipers, J. A. M., 2020, "Comparison of the Local Front Reconstruction Method With a Diffuse Interface Model for the Modeling of Droplet Collisions," Chem. Eng. Sci., **7**, p. 100066.

[270] Brown, D., and Pitt, K., 1972, "Drop Size Distribution of Stirred Non-Coalescing Liquid-Liquid System," Chem. Eng. Sci., **27**(3), pp. 577–583.

[271] Chen, H., and Middleman, S., 1967, "Drop Size Distribution in Agitated Liquid-Liquid Systems," AIChE J., **13**(5), pp. 989–995.

[272] Perlekar, P., Biferale, L., Sbragaglia, M., Srivastava, S., and Toschi, F., 2012, "Droplet Size Distribution in Homogeneous Isotropic Turbulence," Phys. Fluids, **24**(6), pp. 065101–10.

[273] Chatzi, E., and Kiparissides, C., 1994, "Drop Size Distributions in High Holdup Fraction Dispersion Systems: Effect of the Degree of Hydrolysis of PVA Stabilizer," Chem. Eng. Sci., **49**(24), pp. 5039–5052.

[274] Lovick, J., Mouza, A., Paras, S., Lye, G., and Angeli, P., 2005, "Drop Size Distribution in Highly Concentrated Liquid-Liquid Dispersions Using a Light Back Scattering Method," J. Chem. Technol. Biotechnol., **80**(5), pp. 545–552.

[275] Karabelas, A., 1978, "Droplet Size Spectra Generated in Turbulent Pipe Flow of Dilute Liquid/Liquid Dispersions," AIChE J., **24**(2), pp. 170–180.

[276] Brown, W., and Wohletz, K., 1995, "Derivation of the Weibull Distribution Based on Physical Principles and Its Connection to the Rosin-Rammler and Lognormal Distributions," J. Appl. Phys., **78**(4), pp. 2758–2763.

[277] Mugele, R., and Evans, H., 1951, "Droplet Size Distribution in Sprays," Ind. Eng. Chem. Res., **43**(6), pp. 1317–1324.

[278] Deane, G., and Stokes, M., 2002, "Scale Dependence of Bubble Creation Mechanisms in Breaking Waves," Nature, **418**(6900), pp. 839–844.

[279] Deike, L., Melville, W., and Popinet, S., 2016, "Air Entrainment and Bubble Statistics in Breaking Waves," J. Fluid Mech., **801**, pp. 91–129.

[280] Garrett, C., Li, M., and Farmer, D., 2000, "The Connection Between Bubble Size Spectra and Energy Dissipation Rates in the Upper Ocean," J. Phys. Oceanogr., **30**(9), pp. 2163–2171.

[281] Skartlien, R., Sollum, E., and Schumann, H., 2013, "Droplet Size Distributions in Turbulent Emulsions: Breakup Criteria and Surfactant Effects From Direct Numerical Simulations," J. Chem. Phys., **139**(17), p. 174901.

[282] Wang, Z., Yang, J., and Stern, F., 2016, "High-Fidelity Simulations of Bubble, Droplet and Spray Formation in Breaking Waves," J. Fluid Mech., **792**, pp. 307–327.

[283] Chan, W. H. R., Johnson, P., and Moin, P., 2021, "The Turbulent Bubble Break-Up Cascade. Part 1. Theoretical Developments," J. Fluid Mech., **912**, p. A42.

[284] Blenkinsopp, C. E., and Chaplin, J. R., 2010, "Bubble Size Measurements in Breaking Waves Using Optical Fiber Phase Detection Probes," IEEE J. Ocean. Eng., **35**(2), pp. 388–401.

[285] Cartmill, J. W., and Yang, S. M., 1993, "Bubble Size Distribution Under Saltwater and Freshwater Breaking Waves," Dyn. Atmos. Oceans, **20**(1–2), pp. 25–31.

[286] Chan, W. H. R., Johnson, P., Moin, P., and Urzay, J., 2021, "The Turbulent Bubble Break-Up Cascade. Part 2. Numerical Simulations of Breaking Waves," J. Fluid Mech., **912**, p. A43.

[287] Rojas, G., and Loewen, M. R., 2007, "Fiber-Optic Probe Measurements of Void Fraction and Bubble Size Distributions Beneath Breaking Waves," Exp. Fluids, **43**(6), pp. 896–906.

[288] Loewen, M. R., O'Dor, M. A., and Skafel, M. G., 1996, "Bubbles Entrained by Mechanically Generated Breaking Waves," J. Geophys. Res., **101**(C9), pp. 20759–20769.

[289] Chan, W., Dodd, M., Johnson, P., Urzay, J., and Moin, P., 2018, "Formation and Dynamics of Bubbles in Breaking Waves: Part II—The Evolution of the Bubble Size Distribution and Breakup/Coalescence Statistics," Annu. Res. Briefs, pp. 21–34.

[290] Callaghan, A. H., Stokes, M. D., and Deane, G. B., 2014, "The Effect of Water Temperature on Air Entrainment, Bubble Plumes, and Surface Foam in a Laboratory Breaking-Wave Analog," J. Geophys. Res. Oceans, **119**(11), pp. 7463–7482.